

Electric field and van der Waals force induced instabilities in thin viscoelastic bilayers

Dipankar Bandyopadhyay, P. Dinesh Sankar Reddy, and Ashutosh Sharma

Citation: *Phys. Fluids* **24**, 074106 (2012); doi: 10.1063/1.4736549

View online: <http://dx.doi.org/10.1063/1.4736549>

View Table of Contents: <http://pof.aip.org/resource/1/PHFLE6/v24/i7>

Published by the [American Institute of Physics](#).

Related Articles

The final stages of capillary break-up of polymer solutions
Phys. Fluids **24**, 023101 (2012)

Effects of particles on stability of flow-induced precursors
J. Chem. Phys. **136**, 054903 (2012)

Kelvin-Helmholtz instability in viscoelastic fluids in presence of electro-magnetic fields
Phys. Fluids **23**, 094107 (2011)

Electrohydrodynamic instabilities in thin liquid trilayer films
Phys. Fluids **22**, 122102 (2010)

Micromixer based on viscoelastic flow instability at low Reynolds number
Biomicrofluidics **3**, 014106 (2009)

Additional information on Phys. Fluids

Journal Homepage: <http://pof.aip.org/>

Journal Information: http://pof.aip.org/about/about_the_journal

Top downloads: http://pof.aip.org/features/most_downloaded

Information for Authors: <http://pof.aip.org/authors>

ADVERTISEMENT



**Running in Circles Looking
for the Best Science Job?**

Search hundreds of exciting
new jobs each month!

<http://careers.physicstoday.org/jobs>

physicstodayJOBS



Electric field and van der Waals force induced instabilities in thin viscoelastic bilayers

Dipankar Bandyopadhyay,¹ P. Dinesh Sankar Reddy,²
and Ashutosh Sharma^{2,3,a)}

¹*Department of Chemical Engineering, Indian Institute of Technology, Guwahati, India and Centre for Nanotechnology, Indian Institute of Technology, Guwahati, India*

²*Department of Chemical Engineering, Indian Institute of Technology, Kanpur, India*

³*School of Mechanical Engineering, Yeungnam University, Gyongsan, South Korea*

(Received 18 February 2012; accepted 26 June 2012; published online 17 July 2012)

A unified theory is presented for the field-induced spinodal instabilities of thin viscoelastic bilayers composed of the Maxwell fluids or of the soft solids obeying the Kelvin-Voigt model. The analysis includes the different important mechanisms by which a bilayer is rendered unstable: (1) the wetting instability engendered by the excess van der Waals forces in an ultrathin (<100 nm) bilayer (Figure (1a)); (2) the electric field induced instability caused by an external electrostatic field across the bilayer (Figure (1b)); (3) the contact instability caused by the attractive interactions with another surface in the contact proximity of the upper film (Figure (1c)). The key features of the short-, long-, and finite-wavenumber instabilities are compared and contrasted for a host of bilayers having purely viscous, purely elastic, viscoelastic-viscous, and viscoelastic rheological properties. Linear stability analysis shows: (i) controlling mode of instability can shift from one interface to the other, which is accompanied by an abrupt shift in the time and the length scales of the instabilities with the change in the interfacial tensions, relaxation times, and elastic moduli of the films; (ii) purely elastomeric bilayers show a finite wavenumber bifurcation only beyond a critical destabilizing force due to their elastic stiffness; (iii) bilayers with at least one viscous or Maxwell layer show zero elastic-stiffness against the destabilizing influences; (iv) wetting viscoelastic bilayer is unstable only when it is ultrathin and elastically very soft or if one of the layers is purely viscous; (v) Maxwell (elastomer) bilayers show a faster (slower) growth of instability with the increase in relaxation time (elastic modulus). © 2012 American Institute of Physics. [<http://dx.doi.org/10.1063/1.4736549>]

I. INTRODUCTION

Instabilities of thin polymer films have been studied in recent times because of their technological and scientific importance. Fabricating ordered polymer micro/nano structures require an in depth understanding of the stability and dynamics of thin polymer films.¹⁻⁴ As explained below, at least three different important mechanisms of thin film destabilization: dewetting by intermolecular interactions, electric field induced instability, and the contact instability of polymer films, have been investigated previously. These mechanisms can lead to variously self-organized meso-patterns, which can also be spatially ordered by spatio-temporal control of the destabilizing forces. As discussed below, a thin viscoelastic bilayer destabilized by any of the above mechanisms allows much greater variety of patterns and far more flexibility in the control of their morphology. The purpose of this study is to present a unified framework for the analysis of a general viscoelastic bilayer rendered unstable by any of the above three mechanisms and including as limiting cases both purely viscous

^{a)} Author to whom correspondence should be addressed. Electronic mail: ashutos@iitk.ac.in.

liquids and soft solids. The theory allows a seamless understanding of thin film instabilities spanning the destabilizing mechanisms, rheology, long and short length scales, and morphology.

Spinodal dewetting⁵⁻¹³ of an ultrathin (<100 nm) viscous polymer film on a homogeneous substrate is initiated with randomly located circular holes with an average inter-hole distance close to that predicted by the linear stability analysis (LSA). The time and length scales of the hole-formation in an ultrathin (<100 nm) fluid film are governed by the interplay between the stabilizing in-plane curvature forces and destabilizing intermolecular forces. The holes grow with time and coalesce to form a network of ribbon like structures, which further breaks up to produce a collection of droplets. Unlike the spinodal pathway, in heterogeneous nucleation the thin films dewet surfaces by the low-energy passage offered by some pre-existing nucleation sites or defects on the film or substrate.¹⁴⁻¹⁶ Interestingly, periodic defects (physical or chemical) on the substrate can lead to the ordering of the dewetted structures when synchronization between the spinodal wavelength and the periodicity of the substrate pattern takes place.¹⁴⁻²⁴ Previous studies indicate that the slippage^{25,26} of the film on the substrate and the rheological properties²⁷⁻³² of the film can significantly influence the interfacial deformations and subsequent pattern formation.

The self-organizing contact instabilities can also develop periodic patterns on the surface of the soft solid polymer films when its free surface comes in the contact proximity (<100 nm) of another, usually a rigid surface (contactor). The instability becomes readily visible upon separation of adhering surfaces. Previous studies³³⁻⁴⁰ uncovered that this finite-wavenumber, short-wave instability has a length scale (λ) linearly proportional to the film thickness (h), independent of the strength of adhesive inter-surface interactions and the elastic properties. Further, the contact instability at the surface of an elastic film is governed by a competition between the destabilizing inter-surface attractive interactions, such as the van der Waals and electrostatic, and the restoring elastic force in the film. For the sub-micron elastic films, surface tension force also becomes important and the instability wavelength increases depending on a non-dimensional parameter, (γ/Gh), where γ and G are surface tension and elastic shear modulus of the film.³⁹

Apart from the self-organization of thin films under the influence of intermolecular forces, electric field induced instability is another simple and versatile method to fabricate patterns on polymer films. Experiments⁴¹ show that an applied electric field across an initially flat interface of a polymer film can form regular columnar structure when the destabilizing electrostatic stress at the polymer-air interface dominates over the stabilizing curvature force. The electric field induced instabilities of the macroscopic fluid interfaces of thick liquid layers have been known for a long time.⁴²⁻⁴⁵ However, the recent development of the electric field lithographic technique⁴⁶⁻⁶¹ shows that these instabilities in thin polymer films under electric field can lead to interesting meso-patterns such as ordered columns, cavities, and stripes.

As compared to the single layer, the wetting, electric field, and contact instabilities of bilayers are substantially different with a far richer underlying physics. The instabilities of bilayers are initiated by the coupled deformation of a “confined” polymer-polymer interface and a “free” polymer-air surface as shown in Figure 1. In such a scenario, the interfaces can initially deform through either in-phase bending or anti-phase *squeezing* or in a mixed mode as observed for a free film.⁶² These modes grow with time to form interesting interfacial morphologies. Early experimental works⁶³ related to dewetting of polymer bilayers under the influence of intermolecular forces show the importance of the ratios of the polymer viscosities on the dewetting dynamics and interfacial deformations. Subsequent studies^{64,65} have shown the influence of the film thicknesses and viscosity ratios of the film on the hole-formation, movement of the rims surrounding the holes, and the near equilibrium morphologies. Recent experiments on bilayer instabilities uncover a number of interesting aspects such as the possibility of phase inversion,⁶⁶ switching of the instabilities from one interface to the other by changing the film thickness of a bilayer,⁶⁷ and the influence of the patterned substrate.⁶⁸⁻⁷⁰

Danov *et al.*^{71,72} and Paunov *et al.*⁷³ are the first to theoretically show the linear and nonlinear deformations of the bilayer interfaces under the coupled influence of intermolecular forces in addition to the thermal and solutal Marangoni effects. Following this, considering much simpler isothermal and Newtonian bilayer, a number of studies⁷⁴⁻⁸⁵ have identified the length and time scales, and interesting interfacial morphologies at the two interfaces under varied conditions. The

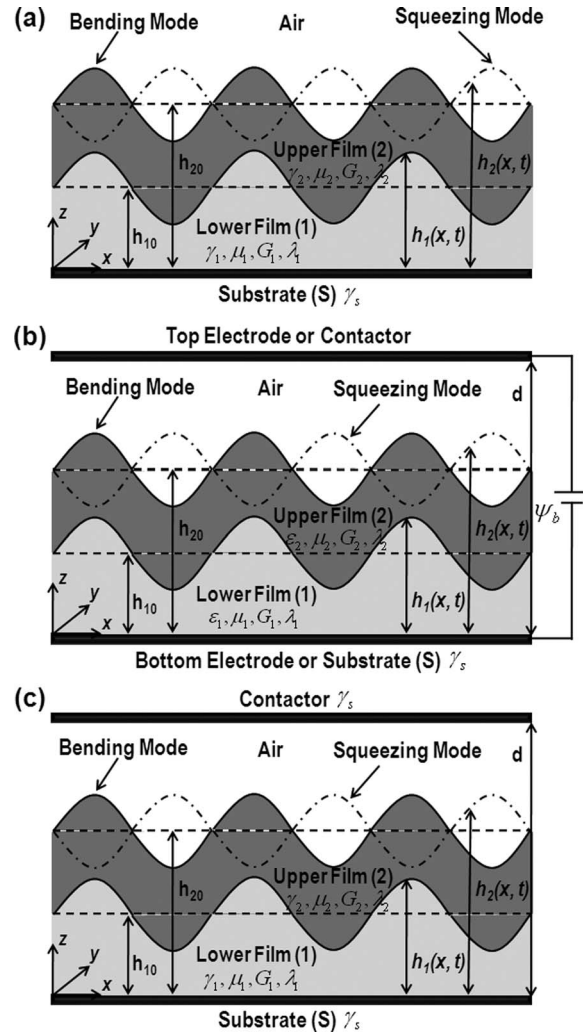


FIG. 1. Schematic diagrams represent (a) “free” bilayer on a solid substrate, (b) bilayer under the influence of electric field, and (c) confined bilayer undergoing contact instability. The solid and the unevenly broken line at the upper interface depict *bending* and *squeezing* mode of evolution with respect to the solid line at the lower interface. The notations γ_i , ε_i , μ_i , G_i , and λ_i represent the surface energy, relative dielectric constant, viscosity, shear modulus, and relaxation time of the i^{th} layer/interface. The notations γ_s and d are the surface energy of the substrate and distance between the electrodes (or between substrate and contactor). The mean and the local thicknesses of the lower (composite) layer are h_{10} and $h_1(x, t)$ (h_{20} and $h_2(x, t)$), respectively.

interfacial morphologies predicted theoretically by these studies have also been validated by some of the recent experiments.^{82,83} The linear and nonlinear analyses on the thermal^{86–88} and solutal Marangoni⁷⁸ instabilities of viscous bilayers, spinodal instabilities of a viscous film resting on a substrate-bonded elastomer film, and a viscous film sandwiched between an elastomer film and a solid substrate are also available in the literature.^{89–91} The experimental and theoretical studies together highlight that, as compared to simpler single films, bilayers are capable of generating self-organized embedded and encapsulated structures with much smaller length scales. Further, a long-range order can be imposed on dewetted structures when the substrates are physically or chemically patterned.^{84,85}

The contact instabilities of thin bilayers have also been studied recently.^{92–95} Unlike the single film scenario, the difference in stiffness of the films in a bilayer adds more flexibility in changing the length scale of the patterns formed at the interface. Even a viscous underlayer is found to impart weak slippage to an elastic top layer and change the length scale significantly.⁹⁵

The experimental studies^{54–56,96,97} on the electric field induced instabilities of bilayers have shown that the different dielectric contrast at the interfaces can lead to interesting embedded and encapsulated patterns, which can be ordered when the spatially varying electric field is imposed employing patterned electrodes. Interestingly, one recent study⁹⁷ shows that the electric field induced instabilities in polymer bilayers can also undergo conditional phase inversion. The theoretical studies^{98,99} show: (i) the embedded structures formed because of these instabilities always have a core with the material of higher dielectric permittivity, (ii) the conditions under which the phase inversion becomes a possibility, and (iii) the possibility of long-range ordering of the structures when the periodicity of electrode-pattern is close to the spinodal length scale of the electric field induced instability. The influence of frequency dependent ac field on the length and time scales as well as on the film morphologies have also been explored in recent theoretical studies.^{100,101}

As noted above, most of the previous studies of bilayers have concentrated on a single mechanism of instability, either the electric field, or the van der Waals dewetting or the contact instability. In addition, often a single rheological description, either purely viscous or purely elastic, is considered. In the present work, the focus is on the analysis valid for all the three destabilizing mechanisms, for rheological descriptions spanning from purely viscous to elastic, and length scales from short to long. Figure 1 shows the different types of bilayers that are described by the unified analysis: (i) “free” bilayer deforming under the influence of intermolecular forces originating with the layers (Figure 1(a)), (ii) a “confined” bilayer deforming under the influence of an electric field (Figure 1(b)), and (iii) “confined” bilayer undergoing deformation because of the interaction between an external contactor and the surface of the upper film (Figure 1(c)). In the formulation, we consider two different types of linear viscoelastic materials—either the Kelvin-Voigt zero-frequency soft materials³⁵ or frequency dependent Maxwell fluids. The former describes a viscoelastic soft solid, whereas the latter describes a viscoelastic liquid. However, it is to be noted that the results obtained from the Kelvin-Voigt model also describe a purely viscous liquid in the limit of vanishing elastic storage modulus. A unified theory has been developed to study the short-, long-, and finite-wavenumber instabilities engendered either by intermolecular forces or by contact forces or by the external electric field, of ultrathin (<100 nm) to thick viscous, elastic, viscoelastic, and viscous-viscoelastic composite bilayers under a single framework. A LSA of this theory uncovers the role of the shear moduli, relaxation times, and dielectric permittivities of the films on the time and the length scales of the instabilities. It may be noted here that the viscoelastic properties of zero-frequency elastomeric materials are very different from the Maxwell fluids. The storage modulus in an elastomeric soft solid is a thermodynamic property, which is a measure of the frequency independent restoring elastic force. The elastomer behaves as a purely elastic solid when the loss modulus is minimal and a viscous behavior is expected when it is elastically very soft.³⁰ In contrast, a Maxwell liquid has no long-term (zero-frequency) elasticity. The magnitude of its relaxation time (ratio of the loss to storage moduli) is a kinetic parameter, which is essentially the time required to dissipate of the stored elastic energy. Thus, LSA of the unified model allows comparison and contrast with the key features of different spinodal instabilities, namely the wetting instability, contact instability, and the electric field induced instability of the bilayers with a wide range of solid-like and liquid-like rheologies. In the case of a single film, rheological properties such as viscosity in a solid model and the relaxation time in a fluid model can be viewed as purely kinetic parameters that play no role in changing the length scale of instability, which is determined by thermodynamic considerations. However, it is known that the length scale of instability in a viscous bilayer can be significantly altered by changing the ratio of viscosities of the films.^{75,80,81} Thus, rheology in a bilayer has more than a purely kinetic role in determining the evolution of two coupled interfaces. In this regard, viscoelasticity in both the layers allows far more flexibility in the control of pattern formation by tailoring the time and length scales over a wide spectrum.

In what follows, we focus on the roles of rheological parameters that define the elastic properties of the two layers. For a viscoelastic liquid, we thus explore the influence of elastic relaxation times in the two layers on the length and time scales of the instabilities. Similarly, in a solid-like bilayer, the roles of elastic storage moduli are considered. The key outcomes from this study can be of significance especially in the areas of mesopatterning of soft materials by self-organization and in control of multilayer coatings.

II. PROBLEM FORMULATION

In this script, x - and z - are the coordinates parallel and normal to the substrate surface (as shown in Figure 1), the bracketed superscript denotes the vector components, the superscript dot represents time derivative of the variable, and the subscripts $i = 1$ and 2 denote the lower and the upper layer/interface. The lower layer, upper layer, and combined film thicknesses are denoted by h_1 , h_3 , and $h_2 (= h_3 + h_1)$, respectively. The respective base state thicknesses are denoted by h_{10} , h_{30} , and h_{20} . The symbols $\sigma_i, \tau_i, \kappa_i, P_i (= p_i - \pi_i), \lambda_i, G_i, \varepsilon_i, \mu_i$, and γ_i are the stress tensor for the elastomer, stress tensor for the Maxwell fluid, curvature, non-body-force pressure, relaxation time, shear modulus, dielectric permittivity, viscosity, and surface energy of the i^{th} layer, respectively, where p_i and π_i denote the isotropic and excess disjoining pressure, respectively because of intermolecular force or electric field. The instability because of the density differences is not considered because for very thin films, the intermolecular forces or the electric field forces dominate significantly over gravity. In addition, owing to the small thicknesses of the films the inertial effects are neglected in the governing equations. Separate formulations for zero-frequency viscoelastic solid and Maxwell fluid are presented because the constitutive relation for the viscoelastic solid is expressed in terms of displacements, $\mathbf{u}_i \{u_i^{(x)}, u_i^{(z)}\}$, whereas for the Maxwell fluid is expressed in terms of the velocities, $\mathbf{v}_i \{v_i^{(x)}, v_i^{(z)}\}$.

A. Zero-frequency linear viscoelastic solid

The following condition for incompressibility, equations of motion, and the constitutive relation describe the dynamics of the i^{th} layer of an incompressible zero-frequency linear viscoelastic solid:

$$\nabla \cdot \mathbf{u}_i = 0, \quad (2.1)$$

$$-\nabla P_i + \nabla \cdot \boldsymbol{\sigma}_i = 0, \quad (2.2)$$

$$\boldsymbol{\sigma}_i = G_i(\nabla \mathbf{u}_i + \nabla \mathbf{u}_i^T) + \mu_i(\nabla \dot{\mathbf{u}}_i + \nabla \dot{\mathbf{u}}_i^T). \quad (2.3)$$

The constitutive relation Eq. (2.3) represents a linear combination of a Newtonian damper and a Hookean elastic spring connected in parallel. The constitutive model is expected to describe the rheology of viscoelastic solid polymer films undergoing a reversible strain under a small load. Previously a number of studies^{30,32,34,90} have shown the usefulness of this model to describe the small deformations of elastomers such as cross-linked PDMS (poly-dimethylsiloxane) under the influence of the intermolecular and electric field forces. Since the bilayer instabilities discussed here are small strain/small deformation problems, this constitutive model is appropriate within the framework of LSA. Interestingly, the model shows correct asymptotic transition to purely elastic material like behavior when the material is elastically very soft (a non-dimensional number, $T = \gamma/Gh < 0.1$).³⁰ The non-dimensional number, T , denotes the importance of surface tension force vis-à-vis the elastic restoring force. A large value of T indicates a negligible role of elasticity and the behavior is thus dominated by the stabilizing effect of surface tension, as in the case of viscous fluids.

The lower layer is considered to be perfectly bonded with the rigid substrate, thus, at $z = 0$, no-slip and non-permeability boundary conditions are enforced,

$$\mathbf{u}_1 = 0. \quad (2.4)$$

The confined liquid/liquid interface at $z = h_1$ is expected to deform under the governing forces. Therefore, continuity of x - and z - components of displacements, normal stress balance, shear stress balance, and the kinematic condition are applied as the boundary conditions,

$$\mathbf{u}_1 = \mathbf{u}_2, \quad (2.5)$$

$$-p_2 + \mathbf{n}_1 \cdot \boldsymbol{\sigma}_2 \cdot \mathbf{n}_1 + p_1 - \mathbf{n}_1 \cdot \boldsymbol{\sigma}_1 \cdot \mathbf{n}_1 = \gamma_{21} \kappa_1, \quad (2.6)$$

$$\mathbf{t}_1 \cdot \boldsymbol{\sigma}_2 \cdot \mathbf{n}_1 = \mathbf{t}_1 \cdot \boldsymbol{\sigma}_1 \cdot \mathbf{n}_1, \quad (2.7)$$

$$\dot{h}_1 + \dot{u}_1^{(x)} (\partial h_1 / \partial x) = \dot{u}_1^{(z)}. \quad (2.8)$$

Here γ_{21} is the interfacial tension at the confined interface is obtained from the relation, $(\sqrt{\gamma_2} - \sqrt{\gamma_1})^2$.^{79–81} In the boundary conditions, the symbols \mathbf{n}_i , $[(-h_{ix}/\sqrt{(1+h_{ix}^2)})1/\sqrt{(1+h_{ix}^2)}]$ and \mathbf{t}_i , $[(1/\sqrt{(1+h_{ix}^2)}, h_{ix}/\sqrt{(1+h_{ix}^2)})]$ represent unit normal and tangent vectors, respectively. The normal stress balance, shear stress balance, and the kinematic condition are applied as boundary conditions at the deformable free surface (liquid/air) at $z = h_2$,

$$-p_2 + \mathbf{n}_2 \cdot \boldsymbol{\sigma}_2 \cdot \mathbf{n}_2 = -\gamma_2 \kappa_2, \quad (2.9)$$

$$\mathbf{t}_2 \cdot \boldsymbol{\sigma}_2 \cdot \mathbf{n}_2 = 0, \quad (2.10)$$

$$\dot{h}_2 + \dot{u}_2^{(x)} (\partial h_2 / \partial x) = \dot{u}_2^{(z)}. \quad (2.11)$$

B. Frequency dependent Maxwell fluid

The conditions for incompressibility, the equations of motion, and the constitutive relation that describe the deformations of the i^{th} layer composed of a Maxwell fluid are

$$\nabla \cdot \mathbf{v}_i = 0, \quad (2.12)$$

$$-\nabla P_i + \nabla \cdot \boldsymbol{\tau}_i = 0, \quad (2.13)$$

$$\boldsymbol{\tau}_i + \lambda_i \dot{\boldsymbol{\tau}}_i = \mu_i (\nabla \mathbf{v}_i + \nabla \mathbf{v}_i^T). \quad (2.14)$$

The expression represents a linear combination of a Newtonian damper and a Hookean elastic spring connected in series. The Maxwell fluids behave like an elastic solid when the time scale for deformation is shorter than the relaxation time and they behave like a Newtonian fluid in the limit of zero relaxation time. In reality, polymeric viscoelastic liquids have a spectrum of relaxation times. Thus, the single relaxation time shown in the constitutive relation Eq. (2.14) can be interpreted as the one corresponding to the frequency (inverse time scale) of fluid motion. Further, the use of a simple time derivative of the stress tensor in the constitutive model instead of the more rigorous upper-convected time derivative arising from the material nonlinearities is justified because we study the spontaneous small deformation of an initially unperturbed bilayer of liquid films under the influence of either intermolecular force or electric field. Moreover, the upper-convected terms are quadratic in the stresses and do not make any linear contributions when expanded about a quiescent base state. Thus, the results obtained from the LSA are exact even with the inclusion of the upper-convected terms.

The lower layer is considered to be perfectly bonded to its rigid substrate and at $z = 0$, no-slip and non-permeability boundary conditions are enforced,

$$\mathbf{v}_1 = 0. \quad (2.15)$$

At the confined interface ($z = h_1$), continuity of x - and z - components of velocities, normal stress balance, shear stress balance, and the kinematic condition are employed as the boundary conditions,

$$\mathbf{v}_1 = \mathbf{v}_2, \quad (2.16)$$

$$-p_2 + \mathbf{n}_1 \cdot \boldsymbol{\tau}_2 \cdot \mathbf{n}_1 + p_1 - \mathbf{n}_1 \cdot \boldsymbol{\tau}_1 \cdot \mathbf{n}_1 = \gamma_{21} \kappa_1, \quad (2.17)$$

$$\mathbf{t}_1 \cdot \boldsymbol{\tau}_2 \cdot \mathbf{n}_1 = \mathbf{t}_1 \cdot \boldsymbol{\tau}_1 \cdot \mathbf{n}_1, \quad (2.18)$$

$$\dot{h}_1 + v_1^{(x)} (\partial h_1 / \partial x) = v_1^{(z)}. \quad (2.19)$$

At the free surface ($z = h_2$), the normal stress balance, shear stress balance, and the kinematic condition are enforced as the boundary conditions,

$$-p_2 + \mathbf{n}_2 \cdot \boldsymbol{\tau}_2 \cdot \mathbf{n}_2 = -\gamma_2 \kappa_2, \quad (2.20)$$

$$\mathbf{t}_2 \cdot \boldsymbol{\tau}_2 \cdot \mathbf{n}_2 = 0, \quad (2.21)$$

$$\dot{h}_2 + v_2^{(x)} (\partial h_2 / \partial x) = v_2^{(z)}. \quad (2.22)$$

C. Excess pressures at the interfaces

1. Wetting instability

The van der Waals disjoining pressures π_1 and π_2 at the interfaces are given by^{74-77,79-81}

$$\pi_1 = -\frac{A_1}{6\pi h_1^3} - \frac{A_2}{6\pi h_2^3}, \quad \pi_2 = -\frac{A_3}{6\pi h_3^3} - \frac{A_2}{6\pi h_2^3}. \quad (2.23)$$

The disjoining pressures are written in terms of effective Hamaker constants, which are derived from the binary Hamaker constants, $A_1 = A_{11} + A_{s2} - A_{s1} - A_{12}$, $A_2 = A_{12} - A_{s2}$ and $A_3 = A_{22} - A_{12}$. The binary Hamaker constants are of the materials denoted by their subscripts s , l , and 2 corresponding to the solid substrate, lower layer, and upper layer, respectively. A positive effective Hamaker constant for a single layer implies an attractive force leading to the wetting instability and its negative value corresponds to thermodynamic stability.

2. Electric field induced instability

The excess pressures at the interfaces resulting from the electric field are modelled by assuming the bilayer with the air gap as a series capacitor as shown in Figure 1(b).^{98,99} The total free energy $\Delta G = -(1/2)C\psi_b^2$ obtained from the capacitance ($C^{-1} = C_1^{-1} + C_2^{-1} + C_a^{-1}$) leads to the following expressions for the excess electrical pressures ($\pi_1 = \partial(-\Delta G)/\partial h_1$ and $\pi_2 = \partial(-\Delta G)/\partial h_3$) at the interfaces,

$$\pi_1 = \left[\frac{-\varepsilon_0 \varepsilon_1 \varepsilon_2 \psi_b^2 ([\varepsilon_2 - \varepsilon_1] + \varepsilon_1 [1 - \varepsilon_2])}{2 [\varepsilon_1 (h_1 + h_3) [\varepsilon_2 - 1] - h_1 [\varepsilon_2 - \varepsilon_1] - \varepsilon_2 \varepsilon_1 d]^2} \right],$$

$$\pi_2 = \left[\frac{-\varepsilon_0 \varepsilon_1^2 \varepsilon_2 \psi_b^2 [1 - \varepsilon_2]}{2 [\varepsilon_1 (h_1 + h_3) [\varepsilon_2 - 1] - h_1 [\varepsilon_2 - \varepsilon_1] - \varepsilon_2 \varepsilon_1 d]^2} \right]. \quad (2.24)$$

The notations $C_1 [= \varepsilon_0 \varepsilon_1 \bar{A} / h_1]$, $C_2 [= \varepsilon_0 \varepsilon_2 \bar{A} / (h_2 - h_1)]$, and $C_a [= \varepsilon_0 \bar{A} / (d - h_2)]$ represent the capacitances of the lower layer, upper layer and air respectively. The symbol ε_0 represents the dielectric permittivity of free space and \bar{A} represents the area of the flat interfaces.

3. Contact instability

In this case, a rigid surface (contactor) interacts with an attractive van der Waals force with the upper surface. The van der Waals disjoining pressures π_1 and π_2 at the two interfaces are given by^{34,39}

$$\pi_1 = 0, \quad \pi_2 = \frac{A}{(d - h_2)^3}, \quad (2.25)$$

where d is the distance between the contactor and the solid substrate as shown in Figure 1(c) and A is the effective Hamaker constant resulting from the interaction between the upper layer and the contactor. The other intermolecular interactions are ignored because in contact instabilities larger film thicknesses (> 100 nm) ensure a weaker contribution from them.

III. LINEAR STABILITY ANALYSIS

In order to perform one dimensional LSA, the two-dimensional governing equations and the boundary conditions are linearized using the normal linear modes, $\mathbf{v}_i = \tilde{\mathbf{v}}_i e^{\omega t + i k x}$, $\mathbf{u}_i = \tilde{\mathbf{u}}_i e^{\omega t + i k x}$, $\boldsymbol{\tau}_{ij} = \tilde{\boldsymbol{\tau}}_{ij} e^{\omega t + i k x}$, $P_i = \tilde{P}_i e^{\omega t + i k x}$, and $h_i = h_{i0} + \tilde{\delta}_i e^{\omega t + i k x}$ where the symbols ω and k represent the linear growth coefficient and the wave number of disturbance, respectively.

A. Zero-frequency linear viscoelastic solid

The governing equations (2.1) to (2.3) are linearized to obtain the following expressions:

$$-ik\tilde{P}_i + (G_i + \mu_i\omega) \left(-k^2\tilde{u}_x^{(i)} + \frac{\partial^2\tilde{u}_x^{(i)}}{\partial z^2} \right) = 0, \quad (3.1)$$

$$-\frac{\partial\tilde{P}_i}{\partial z} + (G_i + \mu_i\omega) \left(-k^2\tilde{u}_z^{(i)} + \frac{\partial^2\tilde{u}_z^{(i)}}{\partial z^2} \right) = 0, \quad (3.2)$$

$$ik\tilde{u}_x^{(i)} + \frac{\partial\tilde{u}_z^{(i)}}{\partial z} = 0. \quad (3.3)$$

Eliminating \tilde{P}_i from the Eqs. (3.1) and (3.2) and then replacing $\tilde{u}_x^{(i)}$ with $-\partial\tilde{u}_z^{(i)}/(ik\partial z)$ from Eq. (3.3) the following biharmonic equation is obtained for the i^{th} ($i = 1$ and 2) layer,

$$\frac{d^4\tilde{u}_z^{(i)}}{dz^4} - 2k^2\frac{d^2\tilde{u}_z^{(i)}}{dz^2} + k^4\tilde{u}_z^{(i)} = 0. \quad (3.4)$$

The general solution of Eq. (3.4) is

$$\tilde{u}_z^{(i)} = (B_{i1} + B_{i2}z)e^{kz} + (B_{i3} + B_{i4}z)e^{-kz}. \quad (3.5)$$

Here the coefficients B_{ij} ($i = 1$ and 2 ; $j = 1$ to 4) are constants. The boundary conditions Eq. (2.4) to (2.11) are also linearized employing the normal linear modes. The following are the linearized no slip and non-permeability conditions at $z = 0$,

$$\tilde{u}_x^{(1)} = \tilde{u}_z^{(1)} = 0. \quad (3.6)$$

The linearized continuity of displacements, the tangential and normal stress balances and the kinematic condition at $z = h_1$ reduces to the form,

$$\tilde{u}_x^{(1)} = \tilde{u}_x^{(2)}, \quad (3.7)$$

$$\tilde{u}_z^{(1)} = \tilde{u}_z^{(2)}, \quad (3.8)$$

$$(G_1 + \mu_1\omega) \left(\frac{\partial\tilde{u}_x^{(1)}}{\partial z} + ik\tilde{u}_z^{(1)} \right) = (G_2 + \mu_2\omega) \left(\frac{\partial\tilde{u}_x^{(2)}}{\partial z} + ik\tilde{u}_z^{(2)} \right), \quad (3.9)$$

$$\begin{aligned} \tilde{P}_1 - \tilde{P}_2 - 2(G_1 + \mu_1\omega)\frac{\partial\tilde{u}_z^{(1)}}{\partial z} + 2(G_2 + \mu_2\omega)\frac{\partial\tilde{u}_z^{(2)}}{\partial z} + \left| \left(-k^2\gamma_{21} + \frac{\partial\pi_1}{\partial h_1} - \frac{\partial\pi_2}{\partial h_1} \right) \tilde{u}_z^{(1)} \right|_{h_{10}, h_{20}} \\ + \left| \left(\frac{\partial\pi_1}{\partial h_2} - \frac{\partial\pi_2}{\partial h_2} \right) \tilde{u}_z^{(2)} \right|_{h_{10}, h_{20}} = 0, \end{aligned} \quad (3.10)$$

$$\tilde{\delta}_1 = \tilde{u}_z^{(1)}|_{h_{10}}. \quad (3.11)$$

The tangential and normal stress balances and the kinematic condition at $z = h_2$ are linearized to

$$(G_2 + \mu_2\omega) \left(\frac{\partial \tilde{u}_x^{(2)}}{\partial z} + ik\tilde{u}_z^{(2)} \right) = 0, \quad (3.12)$$

$$\tilde{P}_2 - 2(G_2 + \mu_2\omega) \frac{\partial \tilde{u}_z^{(2)}}{\partial z} + \left[\left(-k^2\gamma_2 + \frac{\partial \pi_2}{\partial h_2} \right) \tilde{u}_z^{(2)} \right]_{h_{10}, h_{20}} + \left(\frac{\partial \pi_2}{\partial h_1} \right) \tilde{u}_z^{(1)} \Big|_{h_{10}, h_{20}} = 0, \quad (3.13)$$

$$\tilde{\delta}_2 = \tilde{u}_z^{(2)} \Big|_{h_{20}}. \quad (3.14)$$

In the above expressions the disjoining pressures are expanded in Taylor's series about their base states in the following manner:

$$\begin{aligned} \pi_1(h_{10} + \delta_1, h_{20} + \delta_2) &= \pi_1(h_{10}, h_{20}) + \left[(\partial \pi_1 / \partial h_1) \Big|_{h_{10}, h_{20}} \delta_1 + (\partial \pi_1 / \partial h_2) \Big|_{h_{10}, h_{20}} \delta_2 + \dots \right], \\ \pi_2(h_{10} + \delta_1, h_{20} + \delta_2) &= \pi_2(h_{10}, h_{20}) + \left[(\partial \pi_2 / \partial h_1) \Big|_{h_{10}, h_{20}} \delta_1 + (\partial \pi_2 / \partial h_2) \Big|_{h_{10}, h_{20}} \delta_2 + \dots \right]. \end{aligned} \quad (3.15)$$

Here δ_1 and δ_2 are the infinitesimal perturbation at the elastic-viscous and elastic-air interface, respectively. Replacing the expressions for $\tilde{u}_z^{(i)}$, $\tilde{u}_x^{(i)}$, and \tilde{P}_i from the Eqs. (3.1) to (3.3) in the linearized boundary conditions leads to a set of eight homogeneous linear algebraic equations involving eight unknown constants B_{ij} ($i = 1$ and 2 ; $j = 1$ to 4). Equating the determinant of the coefficient matrix of the set of linear equations to zero the dispersion relation for the zero-frequency linear viscoelastic solid bilayer is obtained as shown by the Eq. (A1) in Appendix.

B. Maxwell fluid

The governing equations (2.12) and (2.13) are linearized into the following forms:

$$\tilde{P}_i = \frac{\mu_i}{ik(1 + \omega\lambda_i)} \left(\frac{\partial^2 \tilde{v}_x^{(i)}}{\partial z^2} - k^2 \tilde{v}_x^{(i)} \right), \quad (3.16)$$

$$\frac{\partial \tilde{P}_i}{\partial z} = \frac{1}{1 + \omega\lambda_i} \left(\frac{\partial^2 \tilde{v}_z^{(i)}}{\partial z^2} - k^2 \tilde{v}_z^{(i)} \right), \quad (3.17)$$

$$ik\tilde{v}_x^{(i)} + \frac{\partial \tilde{v}_z^{(i)}}{\partial z} = 0. \quad (3.18)$$

Eliminating \tilde{P}_i from the Eqs. (3.16) and (3.17) and then replacing $\tilde{v}_x^{(i)}$ with $-\partial \tilde{v}_z^{(i)} / (ik\partial z)$ from Eq. (3.18) the following biharmonic equation is obtained for the i^{th} ($i = 1$ and 2) layer,

$$\frac{d^4 \tilde{v}_z^{(i)}}{dz^4} - 2k^2 \frac{d^2 \tilde{v}_z^{(i)}}{dz^2} + k^4 \tilde{v}_z^{(i)} = 0. \quad (3.19)$$

The general solution of Eq. (3.19) is

$$\tilde{v}_i^{(z)} = (C_{i1} + C_{i2}z) e^{kz} + (C_{i3} + C_{i4}z) e^{-kz}. \quad (3.20)$$

Here the coefficients C_{ij} ($i = 1$ and 2 ; $j = 1$ to 4) are constants. The boundary conditions Eq. (2.15) to (2.22) are linearized employing the normal linear modes. The linear no-slip and impermeability boundary conditions at $z = 0$ are

$$\tilde{v}_x^{(1)} = \tilde{v}_z^{(1)} = 0. \quad (3.21)$$

The continuity of velocity components, the tangential and normal stress balances, and the kinematic condition at $z = h_1$ reduce to the form,

$$\tilde{v}_x^{(1)} = \tilde{v}_x^{(2)}, \quad (3.22)$$

$$\tilde{v}_z^{(1)} = \tilde{v}_z^{(2)}, \quad (3.23)$$

$$\tilde{\tau}_{xz}^{(1)} = \tilde{\tau}_{xz}^{(2)}, \quad (3.24)$$

$$\tilde{P}_1 - \tilde{P}_2 - \tilde{\tau}_{zz}^{(1)} + \tilde{\tau}_{zz}^{(2)} + \left| \left(-k^2 \gamma_{21} + \frac{\partial \pi_1}{\partial h_1} - \frac{\partial \pi_2}{\partial h_1} \right) \frac{\tilde{v}_z^{(1)}}{\omega} \right|_{h_{10}, h_{20}} + \left| \left(\frac{\partial \pi_1}{\partial h_2} - \frac{\partial \pi_2}{\partial h_2} \right) \frac{\tilde{v}_z^{(2)}}{\omega} \right|_{h_{10}, h_{20}} = 0, \quad (3.25)$$

$$\tilde{\delta}_1 = \frac{\tilde{v}_z^{(1)}}{\omega} \Big|_{h_{10}}. \quad (3.26)$$

The tangential and normal stress balances and the kinematic condition at $z = h_2$ reduces to the form,

$$\tilde{\tau}_{xz}^{(2)} = 0, \quad (3.27)$$

$$\tilde{P}_2 - \tilde{\tau}_{zz}^{(2)} + \left| \left(-k^2 \gamma_2 + \frac{\partial \pi_2}{\partial h_2} \right) \frac{\tilde{v}_z^{(2)}}{\omega} \right|_{h_{10}, h_{20}} + \left| \left(\frac{\partial \pi_2}{\partial h_1} \right) \frac{\tilde{v}_z^{(1)}}{\omega} \right|_{h_{10}, h_{20}} = 0, \quad (3.28)$$

$$\tilde{\delta}_2 = \frac{\tilde{v}_z^{(2)}}{\omega} \Big|_{h_{20}}. \quad (3.29)$$

Replacing the expressions for $\tilde{v}_z^{(i)}$, $\tilde{v}_x^{(i)}$, and \tilde{P}_i in the linearized boundary conditions results in a set of eight homogeneous linear algebraic equations involving eight unknown constants C_{ij} ($j = 1$ to 4). Equating the determinant of the coefficient matrix of the set of linear equations to zero, we obtain the dispersion relation for the Maxwell bilayer as shown by the Eq. (A2) in Appendix.

The dispersion relation gives, $\omega = f(k)$, when all the physical properties and the thicknesses of the films are known. The dominant growth coefficient (ω_m) and the corresponding wavelength (λ_m) are obtained by finding the global maxima of ω and the corresponding wavelength from the dispersion relations. As a limiting case, we have verified that the dispersion relation for the wetting film reduces to the case of a single viscous film⁵ and a viscous bilayer.^{74,79} The dispersion relations for the elastic bilayers undergoing contact instability^{93,94} and the electric field induced instabilities of the viscous bilayers⁹⁸ are also obtained asymptotically. The operations in this derivation are done with the help of the commercial package MATHEMATICATM.

IV. RESULTS AND DISCUSSION

In this section, the results obtained from the LSA for wetting induced, electric field mediated, and contact instabilities of thin bilayers are discussed. It may be noted that the rheological characteristics of zero-frequency viscoelastic solids are fundamentally different from Maxwell fluids. The storage or elastic modulus in a constant moduli viscoelastic solid is a measure of the frequency independent stabilizing elastic force. When the loss modulus of the viscoelastic solid is very small it behaves like a purely elastic material and its response becomes increasingly faster under an external load. In contrast, when the storage modulus is zero the material behaves like a purely viscous liquid and all the energy supplied is dissipated. A linear viscoelastic solid has a frequency independent, constant loss, and storage moduli. In comparison, a Maxwell liquid has no long-term (zero-frequency) elasticity. The magnitude of its relaxation time (ratio of the loss to storage moduli) is essentially the timescale for the viscous dissipation of the stored elastic energy. Previous studies have shown thermodynamic stabilizing influence of the frequency-independent solid-like elasticity for a linear viscoelastic material.^{30,35} However, increasing the elastic relaxation time in a Maxwell fluid, which is a measure of the fluid elasticity, makes the film kinetically more unstable.^{31,59} Importantly these studies also show that only the rates of deformation and flow are significantly influenced by the

rheological parameters, but the length scale is independent of rheology. More importantly, the length scale of instability for single films is found to be influenced by the thermodynamic parameters such as the dielectric constant, surface tension, and destabilizing intermolecular/electric field forces. As compared to the single film scenario, the length and time scales of instabilities for the bilayers are found to be sensitive towards the kinetic parameter such as viscosity ratio of the films⁸⁰ in addition to the thermodynamic parameters such as ratio of surface tensions at the interfaces, dielectric permittivities of the films, and the intermolecular forces.^{74–76,80,81}

It would help to note a few more general ideas^{7,30,34,34} about the stability of thin films for a clearer interpretation of the results presented below. Instability of viscous liquid films is of a long-wave character ($k_c > k \geq 0$; and $k_c h \ll 1$) and does not require a critical minimum destabilizing force for its inception. However, a thin film of constant elastic modulus material becomes unstable only when the strength of the destabilizing force marginally overcomes the elastic stiffness of the film. For a relatively thick single layer, the instability has a short-wave nature as the critical wavenumber corresponding to this situation follows a wavelength $\sim 3h$, which is independent of the film rheology and surface tension. For very thin sub-micron films, surface tension progressively increases the length scale ($> 3h$), which depends nonlinearly on the surface tension and elastic modulus, eventually reaching the pure viscous surface tension dominated long-wave regime.^{30,39} In comparison to this situation when the destabilizing force is considerably larger than the stabilizing forces, the unstable wavenumbers are bounded between two finite critical wavenumbers. The difference between the critical wavenumbers (instability window) grows with increased destabilization. The dominant wavenumber, k_m displaying the maximum growth rate lies within this window. Extrapolating from what we know about a single film, one can in general anticipate long-wave ($kh \ll 1$) regimes for ultrathin wetting and externally destabilized viscoelastic bilayers where surface tension effects are important. However, a constant elastic modulus should cause a finite wavenumber bifurcation (k_c is nonzero).

The critical wavenumber at the onset of instability and the dominant wavenumber for stronger destabilization are both physically relevant in distinct contexts. In the experiments where an external destabilizing field is progressively ramped up until the film becomes unstable, the critical wavenumber is observed. This happens for example when a contactor gradually approaches the free surface or when an applied electric field is slowly increased. The unstable free surface comes in periodic contact with the contactor/electrode where it is pinned in a meta-stable contact. The experimentally observed length scale of instability in such cases is determined at the bifurcation condition. In the wetting films on the other hand, the van der Waals forces originating within the films are determined only by the film thicknesses. Thus, in an unstable initial configuration beyond the critical, the wavelength corresponds to the dominant mode bounded by the two critical wavenumbers. In view of these reasons, we consider the influence of viscoelasticity both on the critical wavenumber at the onset of instability and on the dominant wavenumber.

In what follows, the major focus is to uncover the effects of the rheological properties such as the ratio of the elastic moduli and relaxation times of the two films in a bilayer. In particular, bilayer film thicknesses are varied from ultrathin to thick to explore the importance of the surface/interfacial tension forces. We thus explore the long- to short-wave instabilities^{30,34,35} in the materials that have solid-like or fluid-like elasticity. In addition, the role of the dielectric permittivities of the films in influencing the length and time scales of the electric field induced instability is also explored.

A. Instabilities of wetting films

Figure 1(a) schematically shows the configuration of a bilayer where the wetting instabilities can be observed because of the presence of intermolecular forces, the most generic of which is the long-range van der Waals force. Importantly, the van der Waals forces can stabilize or destabilize a bilayer depending on the choice of materials for the films. The forces are attractive (repulsive) and destabilizing (stabilizing) when the effective Hamaker constant has a positive (negative) value. In this section, the bilayers are classified based on the macroscopic wetting (dewetting) behavior.^{74,75,79–81}

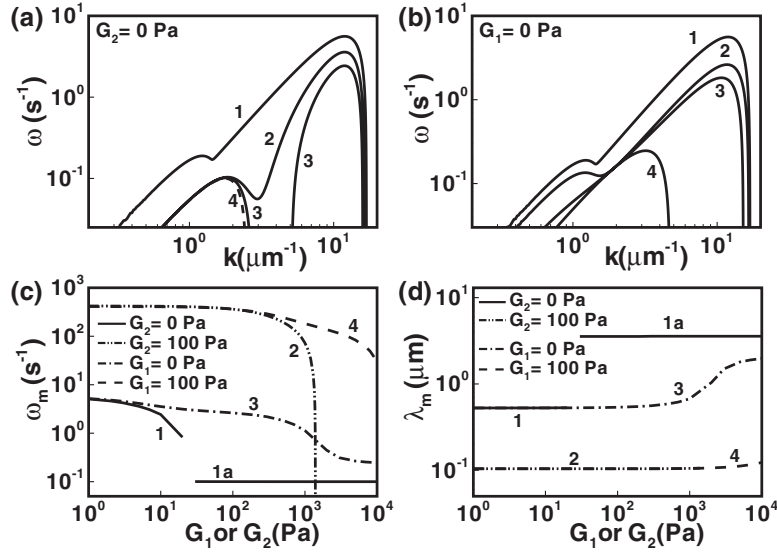


FIG. 2. LSA results for the *case 1* dewetting bilayer. The viscoelastic films in this plot are zero-frequency viscoelastic solids. Plots (a) and (b) show the variation of ω with k . The curves 1–4 in plot (a) correspond to $G_2 = 0$ Pa and $G_1 = 0$ Pa, 5 Pa, 10 Pa, and 10^4 Pa, respectively. In plot (b) curves 1–4 correspond to $G_1 = 0$ Pa and $G_2 = 0$ Pa, 100 Pa, 500 Pa, and 10^4 Pa, respectively. Plots (c) and (d) show the variations of ω_m and λ_m , respectively, (i) with G_1 when $G_2 = 0$ Pa (curve 1) and $G_2 = 100$ Pa (curve 2) and (ii) with G_2 when $G_1 = 0$ Pa (curve 3) and $G_1 = 100$ Pa (curve 4). For curves 2 and 4 in plot (c) and (d) $\gamma_s = 0.8$ N/m. In all the plots, $h_{30} = h_{10} = 10$ nm. All other necessary parameters used in the plots are given in Table I.

The results obtained from the LSA for each case are discussed. The typical parameters employed for the van der Waals forces for different cases are provided in Table I.

1. Case 1 ($A_1 > 0$ and $A_3 > 0$)

This combination of Hamaker constants indicates instability for both the films. The lower layer can be unstable under the influence of $A_1 > 0$ and the upper layer can show instability because of $A_3 > 0$. However, the intermolecular forces have to overcome the stabilizing elastic and capillary forces in the zero-frequency viscoelastic solid films whereas the capillary force is the only resistive force in case of bilayers composed of the Maxwell fluid.

a. Zero-frequency viscoelastic solid. The LSA results for this case are summarized in Figure 2. Figures 2(a) and 2(b) show the variation of the growth coefficient, ω with the wavenumber k when the upper (lower) and lower (upper) layer is viscous (viscoelastic), respectively. Figures 2(c) and 2(d) show the variations of the maximum linear growth coefficient (ω_m) and the corresponding wavelength (λ_m), respectively, with the shear modulus of the lower layer (G_1) at a constant upper layer shear modulus (G_2) and with the shear modulus of the upper layer (G_2) at a constant lower layer shear modulus (G_1). Previous works^{79–81} have shown that a purely viscous bilayer can show a pair of maxima (bimodal behavior) in ω vs. k plots when both the layers are unstable. The nonlinear simulations further showed that the instabilities at the two interfaces can get decoupled and the interfaces then evolve at two different wavelengths.^{80,81} The free surface can grow with a

TABLE I. Typical values used for the van der Waals forces.

System	A_1 (J)	A_2 (J)	A_3 (J)	γ_{21} (N/m)	γ_2 (N/m)	μ_1, μ_2 (Pa s)
Case 1	4.76×10^{-20}	-1.35×10^{-19}	2.05×10^{-20}	0.00385	0.031	1.0
Case 2	-3.81×10^{-22}	5.29×10^{-21}	4.88×10^{-21}	0.0002	0.0362	1.0
Case 3	1.73×10^{-21}	3.18×10^{-21}	-1.33×10^{-20}	0.00385	0.013	0.1

larger wavelength owing its higher surface energy and the confined interface assumes the smaller wavelength because of its smaller stabilizing interfacial tension. We start discussing our results with this interesting bilayer system where the parameters ensure that ω vs. k plots are bimodal (curve 1 in Figure 2(a)) and the lower layer is more unstable. The larger destabilizing intermolecular forces at the lower layer ensures that the dominant mode of instability is at the confined interface and the instability manifests by the larger deformation of the confined interface leading to the rupture of the lower layer.^{80,81} Since the interfacial tension of the confined interface between the two materials is much smaller than the free surface of the bilayer, the dominant mode of instability grows by a larger wavenumber mode corresponding to the lower film. The curves 2-4 in this figure show that when the lower layer is made viscoelastic with progressive increase in the lower layer elasticity, the larger wavenumber dominant mode progressively becomes subdominant. Further, when the lower layer is highly elastic, the smaller wavenumber maximum (longer wavelength) is the dominant mode of instability (curve 4). Increasing elasticity of the viscoelastic lower layer imparts an extra stabilizing influence to the confined interface and beyond a threshold value of shear modulus of the lower layer, the instability evolves by the larger deformation of the viscous upper layer. The shift of the dominant mode of the instability from one interface to the other takes place at the points of the discontinuities shown in the curves 1 and 1a in the Figures 2(c) and 2(d). The changeover of wavelengths from smaller to larger by changing the kinetic parameters such as the ratio of the viscosities in the bilayer films are reported earlier in the literature.⁷⁹⁻⁸¹ Figure 2 uncovers that by changing the extent of elasticity inside the viscoelastic bilayers is another alternative to tune the wavelengths for ultrathin unstable bilayers.

In contrast to the bilayers with a viscous upper layer and a viscoelastic lower layer, the bilayers with a viscoelastic upper layer and a viscous lower layer show completely different instability features. We again start with a purely viscous bilayer with a bimodal instability as shown by curve 1 in Figure 2(b). Curves 2-4 in Figure 2(b) show that with an increase in the elasticity of the upper layer, the ω vs. k plots changes from bimodal to a single dominant mode. Increase in the elasticity of the upper layer synchronizes the deformations at the two interfaces leading to a single dominant mode of instability.

Curve 3 in Figures 2(c) and 2(d) shows that ω_m (λ_m) progressively reduces (increases) with an increase in G_2 , rather than a discontinuous shift as in the previous case. A further inquiry into the ω vs. k plots (not shown here) uncovers that: (i) when at least one of its layers is purely viscous, the bilayer shows a zero elastic stiffness and can thus deform under an infinitesimally small destabilizing field; (ii) the wetting instability of purely viscous or viscoelastic-viscous bilayers have long-wave characteristics ($k_c h \ll 1$) because the dominant wavelength varies in the range of 1 – 10 μm when the film thicknesses are of the order of 10 nm.

As compared to viscous-viscoelastic composite bilayers considered above, when both the layers are viscoelastic the instabilities can have strikingly different characteristics. The curves 2 and 4 in the Figures 2(c) and 2(d) show the results for a viscoelastic bilayer when G_1 is varied at a constant G_2 and G_2 is varied at a constant G_1 , respectively. The key features of instabilities for the viscoelastic bilayers are: (i) the bilayer has a finite elastic stiffness, which leads to a finite-wavenumber instability as found previously for single viscoelastic film.³⁰ The surface tension force stabilizes the smaller waves and the elastic forces stabilize the larger unstable waves. The waves with intermediate length scale can grow under the destabilizing intermolecular forces. This is in contrast to a single viscous film or viscous bilayer or viscous-viscoelastic composite bilayers where the instability can initiate under infinitesimally small destabilizing fields ($\omega \rightarrow 0$ as $k \rightarrow 0$); (ii) only ultrathin films can show wetting instability and stronger destabilizing interactions are necessary to overcome the extra stabilizing elastic forces in both the layers. In the example shown, the solid substrate is considered as a high-energy metal, which gives a higher strength of the van der Waals forces required to engender instability. The analysis predicts a feature size of ~ 100 nm in such a situation; (iii) a bilayer with film thicknesses of 10 nm can undergo wetting instability only when it is very soft with its shear moduli less than a few kPa. Bilayers with higher elasticity cannot be destabilized by the van der Waals interactions; (iv) the dominant growth rate, ω_m progressively decreases with an increase in the elasticity of the films. It is more pronounced when the upper layer has more elastic resistance because the elastic forces at the upper layer stabilizes both the free surface and the confined interface; (v)

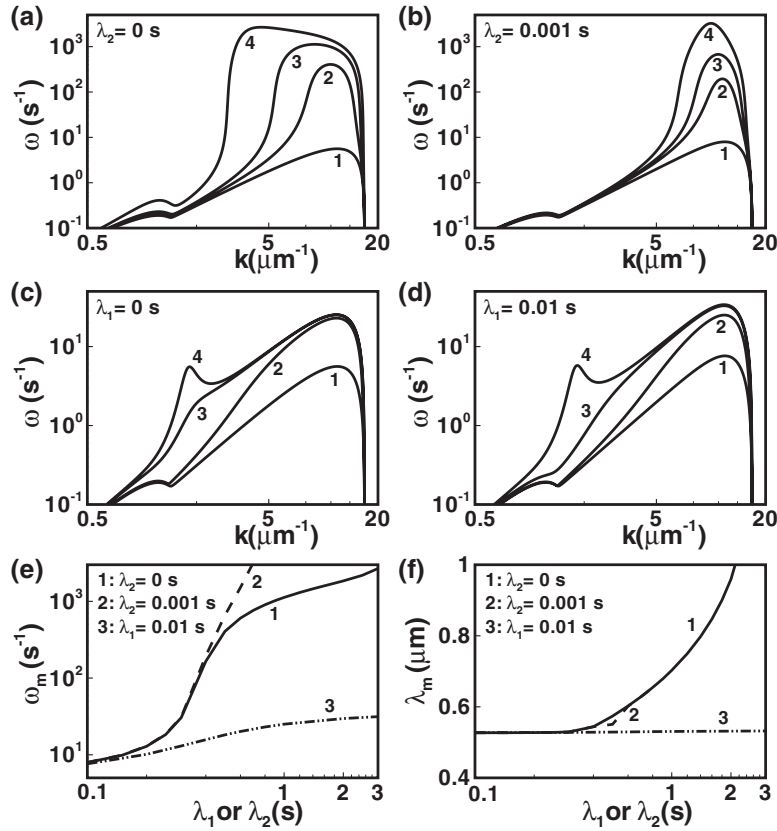


FIG. 3. LSA results for the *case 1*. The viscoelastic films in this plot are Maxwell fluids. Plots (a)–(d) show the variation of ω with k . The curves 1–4 in the plot (a) correspond to $\lambda_2 = 0$ s and $\lambda_1 = 0$ s, 0.5 s, 1.0 s, and 3.0 s. In plot (b) curves 1–4 correspond to $\lambda_2 = 0.001$ s and $\lambda_1 = 0.1$ s, 0.4 s, 0.5 s, and 0.7 s. In plot (c) curves 1–4 correspond to $\lambda_1 = 0$ s and $\lambda_2 = 0$ s, 2 s, 8 s, and 9.5 s. In plot (d) curves 1–4 correspond to $\lambda_1 = 0.01$ s and $\lambda_2 = 0.1$ s, 1 s, 5 s, and 9.5 s. Plots (e) and (f) show the variations of ω_m and λ_m , respectively, (i) with λ_1 when $\lambda_2 = 0$ s (curve 1) and $\lambda_2 = 0.001$ s (curve 2) and (ii) with λ_2 when $\lambda_1 = 0.01$ s (curve 3). For all plots, $h_{30} = h_{10} = 10$ nm. All other necessary parameters used in the plots are given in Table I.

interestingly, λ_m remains almost invariant with the change in the shear moduli of the layers. These observations are important because they indicate: (A) miniaturized elastic-patterns can be developed by employing a bilayer in which destabilizing van der Waals interactions are enhanced and the interfacial tension at the confined interface is reduced, and (B) pattern periodicity can be tuned by changing the elasticity of the two films.

b. Maxwell fluid. In Figure 3, we summarize the LSA results for the bilayers composed of Maxwell fluid. Figures 3(a) to 3(d) show the variation of ω with k , which compare the results for purely viscous, viscoelastic, and viscous-viscoelastic composite Maxwell fluid bilayers. Figures 3(e) and 3(f) show the variations of ω_m and λ_m with the relaxation time of the lower (λ_1) and the upper (λ_2) layers. For the sake of continuity with the above discussion on the zero-frequency viscoelastic bilayer, we examine the same viscous bilayer showing a bimodal instability with a more unstable lower layer. Curve 1 in Figure 3(a) depicts the bimodal nature of the instability with lower layer more unstable because of the dominant larger wavenumber maximum. The curves 2–4 show that when λ_1 is progressively increased under an unstable viscous upper layer, ω_m and λ_m rapidly increase (curve 1 in the Figures 3(e) and 3(f)). The relaxation time in a Maxwell fluid is the measure of the time required to dissipate the elastic-energy stored inside the material. Thus, a layer with a larger relaxation time behaves more like an elastic material for a longer time and ω_m increases rapidly with an increase in the relaxation times of the lower layer. It may be noted here that increase in λ_1 has a greater effect in enhancing the larger wavenumber maximum as compared to the smaller wavenumber maximum.

The ω vs. k plots for the bilayers with very large relaxation times approaching the viscous time scale show divergence ($\omega \rightarrow \infty$) near the dominant wavenumber (results not shown). This phenomenon has been discussed previously for a single Maxwell film.³¹ The fast elastic dynamics in such cases can be resolved by the inclusion of the inertial effects as shown in the work by Tomar *et al.*³¹

In contrast to the bilayers with a viscous upper layer and a viscoelastic lower layer, the bilayers with a viscoelastic upper layer on a viscous lower layer show a completely different behavior when λ_2 is increased. The curves 2-4 in the Figure 3(c) depicts the smaller wavenumber maximum grows faster than the larger wavenumber maximum and can become the dominant mode at higher λ_2 . It may be noted that the smaller wavenumber maximum also diverges at very high values of λ_2 indicating the requirement of the inertial time scale in the formulation to remove the non-physical singularity introduced by a faster elastic time scale (results not shown).

Figures 3(b), 3(d) and curves 2 and 3 in Figures 3(e) and 3(f) summarizes the key features of the wetting instability when both the layers are viscoelastic: (i) The increase in the growth rate of instability is more explosive when the lower layer relaxation time is increased (curve 2 in Figure 3(e)); (ii) increasing the relaxation time of the more unstable upper layer only increases the growth rate of instability and the length scale remains unaltered (curve 3 in Figure 3(f)); (iii) increasing the relaxation time of the upper layer on a viscoelastic lower layer can cause shifting of dominant mode of instability from the confined interface to the free surface as shown by the curves 2-4 in the Figure 3(d). This shift is also accompanied by an abrupt change in the wavelength of instability; (iv) unlike the purely viscoelastic bilayers with elastomeric solids, which show a finite wavenumber instability, the Maxwell bilayers show a long-wave ($k_c > k \geq 0$ and $k_c h \ll 1$) wetting instability.

The results shown in the Figures 2 and 3 clearly indicate that unlike a single film where the parameters such as relaxation time and shear modulus can merely change the time scale of the wetting instability, for bilayers both the time and length scales can be significantly altered by tuning the ratios of the rheological properties.

2. Case 2 ($A_1 < 0$ and $A_3 > 0$)

In this case, the upper layer can be unstable ($A_3 > 0$) on a stable ($A_1 < 0$) lower layer. However, the instability in the upper layer can grow either by a dominant deformation at the confined interface or at the free surface. The influence of the relaxation times and shear moduli of the films can completely change the evolution of instability by restricting or promoting the destabilizing forces present in the films. Figure 4 summarizes the LSA results for this case.

a. Zero-frequency linear viscoelastic solid. Figure 4(a) shows the variation of ω with k , and Figures 4(b) and 4(c) show the variations of the dominant parameters, ω_m and λ_m with the change in the G_1 and G_2 . It may be noted here that in the physically realistic cases, the van der Waals forces cannot be made sufficiently strong to engender instability in the bilayers when both the layers are viscoelastic solids unless their shear moduli and the film thickness are very small.³⁰

Thus, only the results for the viscous-viscoelastic bilayers are shown. Curve 1 in Figure 4(a) corresponds to a purely viscous bilayer. Unlike the case 1 bilayers, the nature of van der Waals forces in the films in this case ensures only the upper layer is unstable. The bimodal nature of this curve indicates that the dominant mode of instability can reside on any of the two interfaces present, which can break the upper film in long time. In curve 1, the low interfacial tension ensure that the dominant large wavenumber mode stays at the confined interface. Curves 2 and 3 show that when the elasticity of the lower layer is increased and the deformation of the confined interface is restricted, the growth rate decreases as shown by the curve 1 in Figure 4(b). Eventually, the small wavenumber mode becomes dominant (curve 3 in Figure 4(a)) and the instability grows by the deformation of the free surface with larger λ_m as shown by the curve 1a in the Figure 4(c).

In contrast, starting with a viscous bilayer and increasing the elasticity of the upper viscoelastic film show a different picture. The curves 1, 4, and 5 in Figure 4(a) show that when the elasticity of the upper layer is increased, the confined interface and the free surface gets progressively coupled. Thus, a bilayer with a high shear modulus of the upper layer and a viscous lower layer displays a single mode in the ω vs. k plot (curve 5 in Figure 4(a)). The curves 2 in the Figures 4(b) and

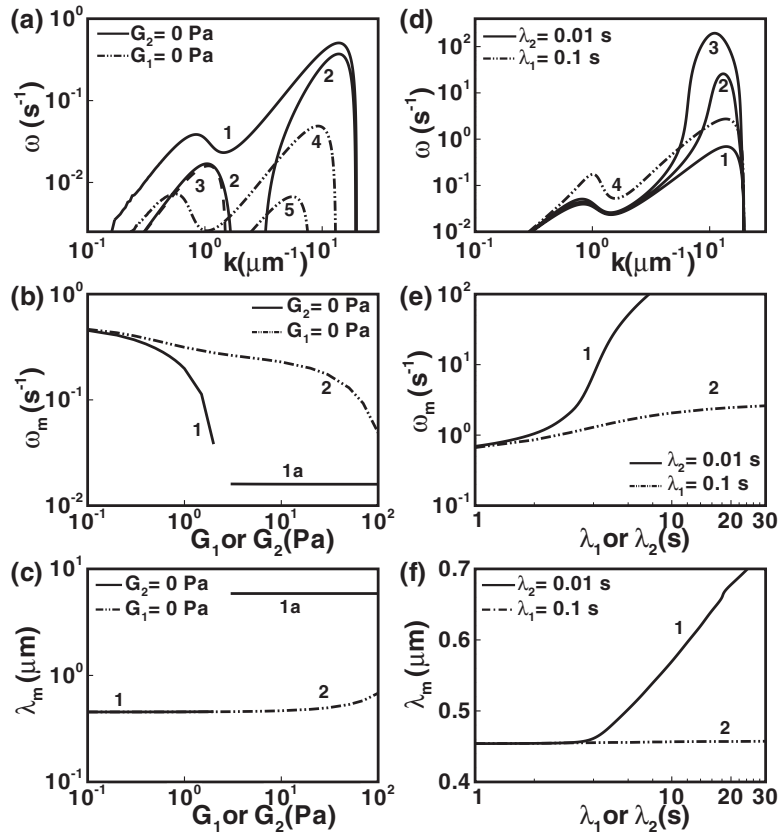


FIG. 4. LSA results for the *case 2*. The viscoelastic films in plots (a)–(c) are for zero frequency viscoelastic solids and (d)–(f) are for Maxwell fluids. Plots (a) and (d) show the variation of ω with k . In plot (a), the curves 1–3 correspond to $G_2 = 0$ Pa and $G_1 = 0$ Pa, 0.3 Pa, and 10 Pa, respectively. The curves 4 and 5 correspond to $G_1 = 0$ Pa when $G_2 = 100$ Pa and 150 Pa, respectively. The curves 1–3 in the plot (d) correspond to $\lambda_2 = 0.01$ s when $\lambda_1 = 1.0$ s, 5.0 s, and 10.0 s, respectively. The curve 4 corresponds to $\lambda_1 = 0.1$ s and $\lambda_2 = 50$ s. Plots (b) and (c) [(e) and (f)] show the variations of ω_m and λ_m , respectively, (i) with G_1 when $G_2 = 0$ Pa (curve 1) and (ii) with G_2 when $G_1 = 0$ Pa (curve 2) [(i) with λ_1 when $\lambda_2 = 0.02$ s (curve 1) and (ii) with λ_2 when $\lambda_1 = 0.1$ s (curve 2)]. For all plots, $h_{30} = h_{10} = 10$ nm. All other necessary parameters used in the plots are given in Table I.

4(c) more clearly show that when the upper layer is viscoelastic, ω_m progressively reduces whereas λ_m remains almost constant with the change in G_2 . The plots indicate that for a wetting bilayer with an unstable viscoelastic (viscous) upper layer on a stable viscous (viscoelastic) lower layer the wavelength can be tuned from a few hundred nanometres to a few microns by changing the shear modulus of the lower layer.

b. Maxwell fluid. The LSA results for the Maxwell fluids in this case are discussed in the Figures 4(d)–4(f). Figure 4(d) shows the variation of ω with k , and Figures 4(e) and 4(f) show the variations of ω_m and λ_m with the change in the λ_1 and λ_2 . Since the Maxwell fluids are more prone to destabilization owing to which the fluid bilayers show some new and interesting features. Curve 1 in Figure 4(d) show a bimodal instability for a viscous bilayer with unstable upper layer on a stable lower layer. A shorter dominant wavelength indicates that the confined interface is more unstable. The curves 1-3 in Figure 4(d) show that with increase in λ_1 the larger wavenumber maximum increases rapidly. Thus, increase in relaxation time at the lower layer leads to a faster destabilizing confined interface, which can lead to the rupture of the upper layer in long time. In contrast, curve 4 shows a different scenario when λ_2 is increased. In such a situation, the increased relaxation time at the upper layer equally destabilizes the free and the confined interfaces. Thus, both the modes in the bimodal plot show an enhanced growth rate. However, the plots also show that λ_1 plays a primary role in strengthening the instability when compared to λ_2 .

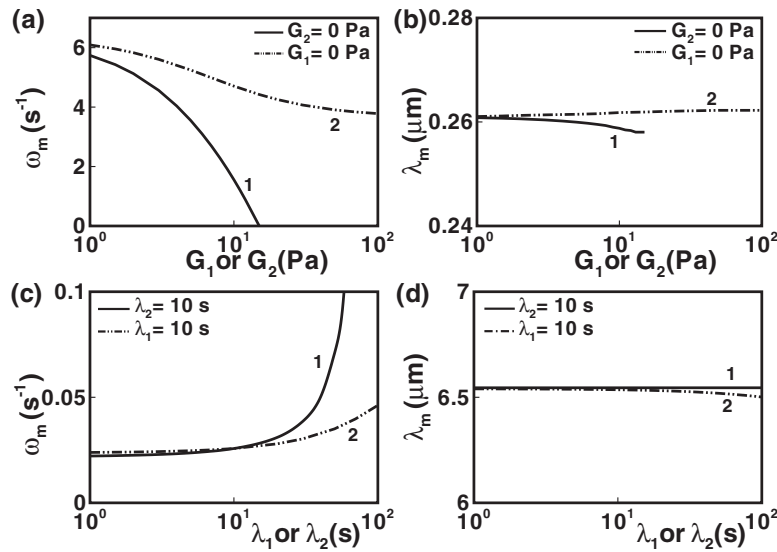


FIG. 5. LSA results for the case 3. For zero frequency viscoelastic solids, plots (a) and (b) show the variations of ω_m and λ_m , respectively, (i) with G_1 when $G_2 = 0$ Pa (curve 1) and (ii) with G_2 when $G_1 = 0$ Pa (curve 2). Plots (c) and (d) show the variations of ω_m and λ_m , respectively, for Maxwell fluids (i) with λ_1 when $\lambda_2 = 10$ Pa (curve 1) and (ii) with λ_2 when $\lambda_1 = 10$ s (curve 2). For plots (a) and (b), $h_{30} = h_{10} = 2.0$ nm. For plots (c) and (d), $h_{30} = h_{10} = 10$ nm. All other necessary parameters used in the plots are given in Table I.

3. Case 3 ($A_1 > 0$ and $A_3 < 0$)

In this case, the lower layer is unstable because $A_1 > 0$ and the upper layer is stable on the lower layer because $A_3 < 0$. Thus, we expect this bilayer to behave more like a single film because of a more passive upper layer. An interesting aspect of this case is that the free surface of the stable upper layer can trace the contours of the structures formed at the confined interface, thus providing a pathway for the inter-surface pattern replication and transfer.⁸¹ In addition, the presence of the upper layer reduces the interfacial tension at the confined interface, which can lead to a reduction in the wavelength as shown previously by employing the LSA and nonlinear simulations.^{80,81}

a. Zero-frequency linear viscoelastic solid. Figures 5(a) and 5(b) summarize the LSA results for this case where one of the layers is purely viscous and the other one is viscoelastic. Figure 5(a) shows that increase in the shear modulus of either of the films leads to a reduction in ω_m , whereas λ_m remains almost constant. Increasing G_1 has more stabilizing influence as can be observed in the curve 1 in the Figure 5(a) because larger G_1 resists any deformation of the unstable lower layer to make the system stable.

b. Maxwell fluid. In contrast to the viscoelastic solid case, Figures 5(c) and 5(d) show that increase in the relaxation times of the layers can strengthen the instability. It is observed that when the relaxation times of both the layers are simultaneously increased, the growth rate increases more than when the individual relaxation times of the layers are increased one at a time. Figure 5(d) confirms that the wavelength of instability does not change much with the change in the relaxation times of the films in this case.

Bilayers for this case behave much like a single film with similar characteristics: (i) very thin and soft films are unstable when the lower layer is a Kelvin-Voigt zero-frequency soft material, whereas thicker films can be unstable when the lower film is a Maxwell fluid; (ii) the wavelength of instability is insensitive to the shear modulus or the relaxation times.

B. Electric field induced instabilities

The application of an electrostatic field across the interfaces of a bilayer (Figure 1(b)) of dielectric materials generates additional stresses because of the induced charge separation near the

TABLE II. Typical values used for the electric field instability.

$\epsilon_0(\text{C}^2/\text{N m}^2)$	$\psi(\text{V})$	$\gamma_{21}(\text{N/m})$	$\gamma_2(\text{N/m})$	$\mu_1, \mu_2(\text{Pa s})$	$d(\text{nm})$	$h_{10}(\text{nm})$	$h_{30}(\text{nm})$
8.85×10^{-12}	150	0.0007	0.03	1	1000	150	100

interfaces. The bulk is always electro neutral for the purely dielectric bilayers. To minimize the excess free energy because of the charge separation at the interface arising from the applied field, the free surface of a bilayer always deforms more in the direction of the upper electrode because of the larger dielectric constant of the upper layer compared to air that it displaces. However, the confined interface can deform in either direction depending upon the difference in the dielectric constants of the two films ($\epsilon_1 > \epsilon_2$ or $\epsilon_1 < \epsilon_2$). The hydrodynamic factors play an important role in the growth of instability. For example, an increase in the strength of the elastic, viscous or capillary forces leads to a slower kinetics of destabilization whereas an increase in the relaxation time of the material leads to a faster growth of the instabilities. The wetting film discussed above can be unstable only when it is ultrathin (< 100 nm) because the fast decay of the intermolecular forces. However, electric field can engender instability in the films of any thickness. In this section, we discuss the LSA results of the electric field induced instabilities in the ultrathin to thick viscoelastic bilayers. In particular, we demonstrate the role of the interfacial, rheological, and electrical properties of the films on the time and length scales of instabilities. The typical parameters employed for the plots related to the electric field induced instabilities are provided in the Table II.

1. Influence of dielectric properties

The electrical properties of the films play a crucial role in the stress distribution across the interfaces. Here we discuss the influence of the dielectric permittivities on the length and time scales of instabilities in the linear viscoelastic bilayers. The permittivity of a dielectric medium is a measure of its ability to polarize induced dipoles in presence of an external electric field. To extract the influence of dielectric properties, the elastic modulus and the relaxations times of the films are kept similar in all the figures.

a. Zero-frequency linear viscoelastic solid. Figure 6 shows the LSA results for this case. Figure 6(a) shows ω vs. k plots and Figures 6(b) and 6(c) show the variations of ω_m and λ_m with the ratio of the dielectric permittivities, $E_r (= \epsilon_2/\epsilon_1)$. Curve 1 in Figure 6(a) shows that when the dielectric-contrast between the viscoelastic layers is high, a larger electrical stress and lower interfacial tension at the confined interface ensure a large wavenumber dominant mode of instability. In such a situation, the instability evolves by a larger deformation of the confined interface. It may be noted here that these finite-wavenumber electric field induced instabilities of thin viscoelastic bilayers originate only beyond a critical value of the electric field when the destabilizing electric field induced stresses overcome the stabilizing elastic and capillary forces. Decrease in the dielectric-contrast between the layers (curves 2 to 4) causes a reduction in the electric field induced stress at the confined interface which results in: (i) decrease in the growth rate of instability (curve 1 in Figure 6(b)) and, (ii) shift of the dominant mode from the larger wavenumber (shorter wavelength) to the shorter wavenumber (larger wavelength) mode (curves 1a and 1 in Figure 6(c)). The shifting of the dominant mode is reflected in the discontinuities of the curves shown in Figures 6(b) and 6(c).

Interestingly, when the electric field induced stresses at the confined and free interfaces are comparable to the stabilizing elastic and surface tension forces, a bimodal instability curve is observed as shown in the curves 2 and 3 of Figure 6(a). In such situation, the two interfaces are found to evolve with two different wavelengths.^{98,99} Here, the larger (smaller) wavelength mode corresponds to the free (confined) surface because of the larger (smaller) interfacial tension as compared to the confined interface (free surface). Figures 6(b) and 6(c) more clearly show that when the dielectric-contrast is high because of either $\epsilon_2 \ll \epsilon_1$ (curve 1a, at low E_r) or $\epsilon_2 \gg \epsilon_1$ (curve 2a, at high E_r), the dominant mode of instability is at the confined interface and the wavelength

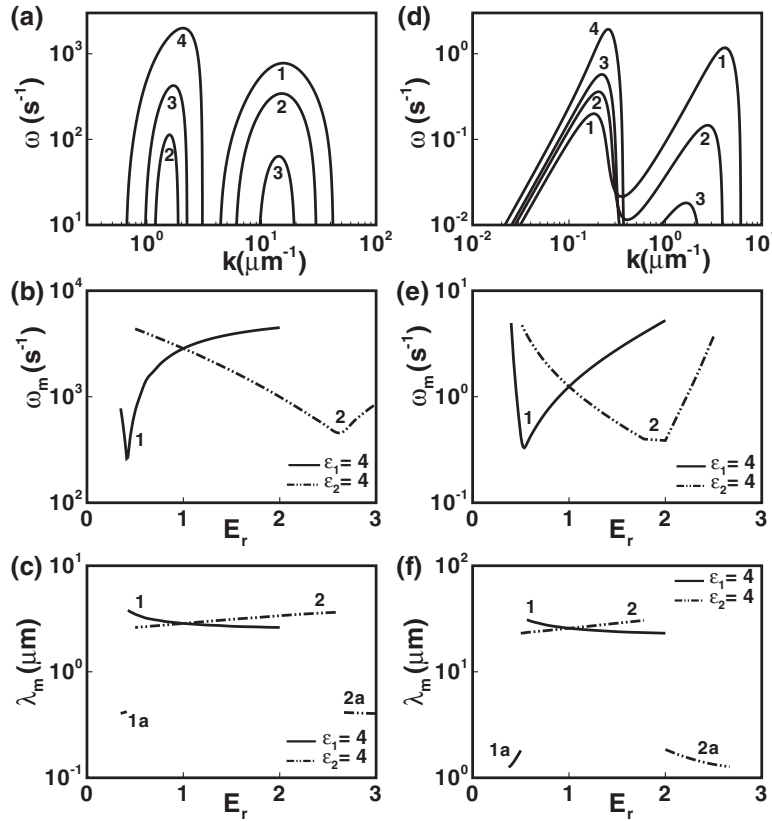


FIG. 6. LSA results for viscoelastic bilayers under the influence of electrical fields. Plots (a)-(c) are for zero frequency viscoelastic solids when $G_1 = 1000$ Pa, $G_2 = 100$ Pa, and $\psi_b = 200$ V. Plots (d)-(f) are for Maxwell fluids when $\lambda_1 = 1.0$ s, $\lambda_2 = 0.1$ s, and $\psi_b = 20$ V. Plots (a) and (d) show the variation of ω with k . The curves 1–4 in plot (a) correspond to $\varepsilon_2 = 1.4, 1.6, 1.8,$ and 3.0 , respectively, at constant $\varepsilon_1 = 4.0$. The curves 1–4 in plot (d) correspond to $\varepsilon_2 = 1.8, 2.25, 2.75,$ and 5.0 , respectively, at constant $\varepsilon_1 = 4.0$. Plots (b) and (e) show the variation of ω_m with $E_r (= \varepsilon_2/\varepsilon_1)$. Plots (c) and (f) show the variation of λ_m with $E_r (= \varepsilon_2/\varepsilon_1)$. In all the plots $\gamma_{12} = 0.000015$ N/m. The other necessary parameters used in the plots are given in Table II.

of instability is smaller. However, for intermediate values of E_r , both the curves 1 and 2 show that, the dominant mode shifts to the free surface and the instability grows with a larger wavelength.

The results shown in Figure 6 clearly depict a shift in the controlling interface accompanied by a switchover of the wavelength when the dielectric permittivities of the layers are tuned. The phenomenon is also associated with the change in the length scale as discussed for the wetting instability. It may be noted that similar to the wetting bilayers, the Kelvin-Voigt soft bilayers under electric field also show a finite elastic stiffness and show a finite wavenumber instability (not shown here). The soft solids undergo deformation only beyond a critical strength of the external field.

b. Maxwell fluid. Interestingly, a Maxwell fluid is also found to respond in the similar manner when the dielectric-contrast between the viscoelastic films is varied. The only difference for a Maxwell bilayer is that the films have zero elastic stiffness and the instabilities can initiate under the influence of a vanishingly small external field ($k_c = 0$), as compared to the finite-wavenumber instability in the zero-frequency viscoelastic bilayers. Figure 6(d) shows ω vs. k plots and Figures 6(e) and 6(f) show the variations of ω_m and λ_m with $E_r (= \varepsilon_2/\varepsilon_1)$. Curve 1 in Figure 6(d) shows that when the dielectric-contrast between the viscoelastic layers is high, the confined interface evolves with a large wavenumber dominant mode of instability. With progressive reduction in the dielectric-contrast between the layers (curves 2 to 4), the growth rate of instability reduces (curve 1 in Figure 6(e)) and the dominant mode shifts from the larger to shorter wavenumber mode (curves 1a

and 1 in Figure 6(f). Again, the shift occurs by the bimodal nature of the instability as observed in the curves 2 and 3 in Figure 6(d). Figures 6(e) and 6(f) clearly show that when the dielectric-contrast is very high, either $\varepsilon_2 \ll \varepsilon_1$ (curve 1a, at low E_r) or $\varepsilon_2 \gg \varepsilon_1$ (curve 2a, at high E_r), the dominant mode of instability is at the confined interface and the wavelength of instability is smaller. However, the dominant mode shifts to the free surface and the instability grows with a larger wavelength for the intermediate values of E_r .

A comparison between the results obtained for the Kelvin-Voigt soft materials and Maxwell bilayers under electric field leads to the following observations: (i) the Maxwell bilayers can deform faster and at much lower external fields; (ii) when the dominant mode is at the confined interface, a short-wave (500 nm to 1 μm) instability is expected even when the films are fairly thin (100 nm to 150 nm); (iii) Maxwell material behaves elastically with instantaneous response when its relaxation time is comparable to the viscous time scale, which is shortened by imposition of large destabilizing fields. In such cases, the elastic inertia needs to be included in the analysis to capture the fast time scale.

2. Influence of rheological properties

Figures 7 and 8 summarize the results for the bilayers with fixed dielectric constants and varying rheological properties. Starting with a viscous bilayer, we demonstrate the influence of the shear modulus and the relaxation times of the films on the growth rate and wavelength of instability.

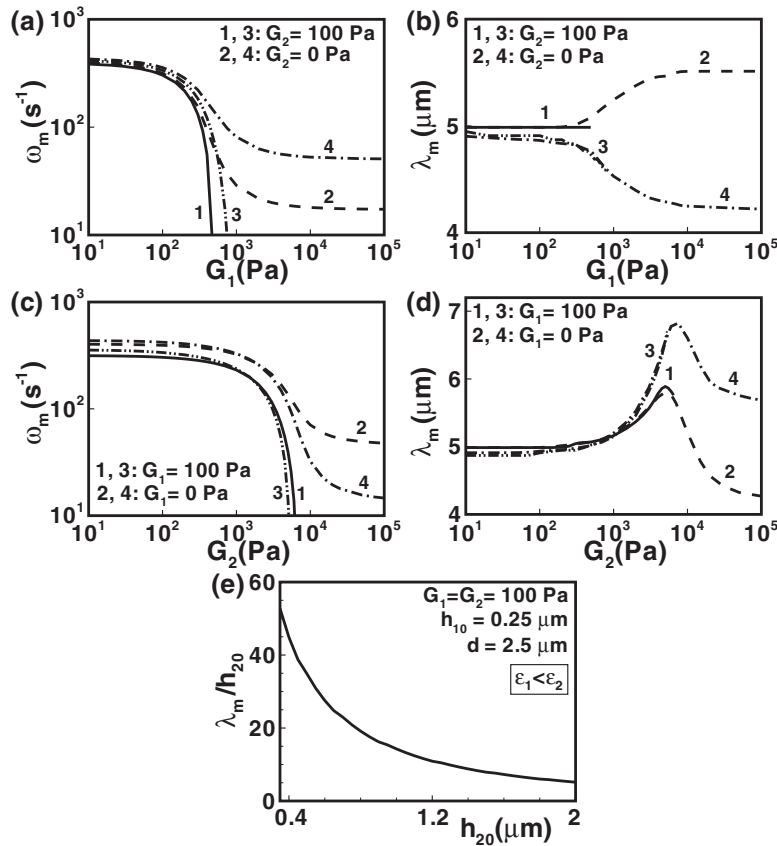


FIG. 7. LSA results for zero frequency viscoelastic solid bilayers under the influence of electrical fields. Plots (a) and (b) [(c) and (d)] show the variation of ω_m and λ_m with G_2 [λ_2]. The curves 1 [3] in (a) and (b) represent $G_2 = 100$ Pa and the curves 2 [4] represent $G_2 = 0$ Pa when $\varepsilon_1 (=3.0) > \varepsilon_2 (=2.0)$ [$\varepsilon_1 (=2.0) < \varepsilon_2 (=3.0)$]. The curves 1 [3] in (c) and (d) represent $G_1 = 100$ Pa and the curves 2 [4] represent $G_1 = 0$ Pa when $\varepsilon_1 (=3.0) > \varepsilon_2 (=2.0)$ [$\varepsilon_1 (=2.0) < \varepsilon_2 (=3.0)$]. Plot (e) shows the variation of λ_m/h_{20} with h_{20} when $G_1 = G_2 = 100$ Pa. All other necessary parameters used in the plots are given in Table II.

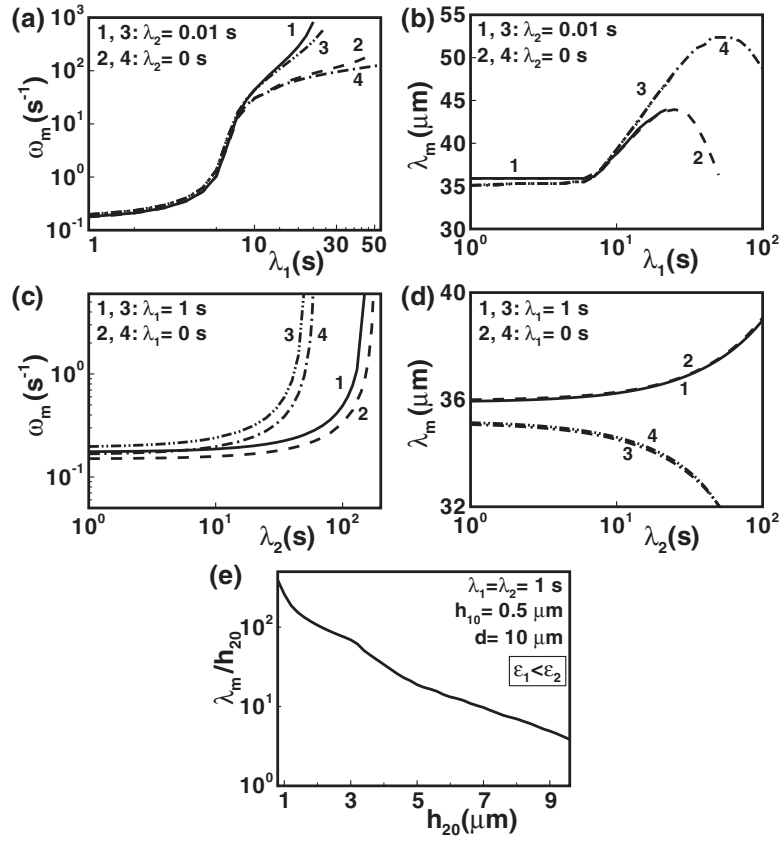


FIG. 8. LSA results for Maxwell fluid bilayers under the influence of electrical fields. Plots (a) and (b) [(c) and (d)] show the variation of ω_m and λ_m with λ_1 [λ_2]. The curves 1 [3] in (a) and (b) represent $\lambda_2 = 0.01$ s and the curves 2 [4] represent $\lambda_2 = 0$ s for $\varepsilon_1 (=3.0) > \varepsilon_2 (=2.0)$ [$\varepsilon_1 (=2.0) < \varepsilon_2 (=3.0)$]. The curves 1 [3] in (c) and (d) represent $\lambda_1 = 1$ s and the curves 2 [4] represent $\lambda_1 = 0$ s for $\varepsilon_1 (=3.0) > \varepsilon_2 (=2.0)$ [$\varepsilon_1 (=2.0) < \varepsilon_2 (=3.0)$]. For all the plots $\psi_b = 20$ V. Plot (e) shows the variation of λ_m/h_{20} with h_{20} when $\lambda_1 = \lambda_2 = 1$ s when $\psi_b = 100$ V. All other necessary parameters used in the plots are given in Table II.

a. Zero-frequency linear viscoelastic solid. Figures 7(a) and 7(b) show the variations of ω_m and λ_m with G_1 and Figures 7(c) and 7(d) show the same with G_2 . Curves 1 ($\varepsilon_2 < \varepsilon_1$) and 3 ($\varepsilon_2 > \varepsilon_1$) in all the figures show that when the shear modulus of one of the layers is increased for a bilayer with two viscoelastic films, ω_m rapidly reduces in a narrow window of G to impart greater thermodynamic stability. Beyond a finite critical stiffness of the elastomer films (higher G), the bilayer becomes thermodynamically stable. In contrast, the curves 2 ($\varepsilon_2 < \varepsilon_1$) and 4 ($\varepsilon_2 > \varepsilon_1$) in all the figures show that when only one of the films of the bilayer is viscoelastic and the other is viscous, the reduction in ω_m is not catastrophic with increase in the shear modulus of the viscoelastic film. This is because even though the elasticity imparts greater stability to the viscoelastic film, the viscous film remains unconditionally unstable.

Thus, the bilayers with one viscous layer show a zero elastic stiffness against the destabilizing electric field. Importantly, when G_1 is increased when the upper layer is viscous, λ_m shifts from lower to higher values when $\varepsilon_2 < \varepsilon_1$ (curve 2 in Figure 7(b)). However, curve 4 in Figure 7(b) shows that λ_m shift from the higher to lower values when $\varepsilon_2 > \varepsilon_1$. As discussed previously for the other cases, the shift of λ_m is again associated with the switchover of the dominant mode of instability from the confined interface to the free surface. The variation in λ_m is more pronounced when the lower layer is viscous and G_2 is progressively increased as shown by the curves 2 and 4 in the Figure 7(d). This is because an increase in the upper layer elasticity affects deformations at both the interfaces. Figure 7(e) shows that the electric field induced instabilities of the viscoelastic bilayers can undergo a long- to short-wave transition as the film thickness is changed from a few hundred nm (thin) to a

few microns (thick). This is similar to the single layer scenario.³⁰ For ultrathin bilayers, the dominant influence of the surface tension shifts the length scale to the long-wave regime. However, as the film thickness is progressively increased, the influence of surface tension decreases leading to the transition from the long- to short-waves.

b. Maxwell fluid. Figures 8(a) and 8(b) show the variations of ω_m and λ_m with λ_1 and Figures 8(c) and 8(d) show the same with λ_2 . Curves 1 ($\varepsilon_2 < \varepsilon_1$) and 3 ($\varepsilon_2 > \varepsilon_1$) in all the figures show that when the relaxation time of one of the layers is increased for a bilayer with viscoelastic films, ω_m rapidly increases and kinetically destabilizes the system.

Increase in relaxation time promotes a faster response to the destabilizing electric field, which imparts stronger instability to the bilayer. In contrast, the curves 2 ($\varepsilon_2 < \varepsilon_1$) and 4 ($\varepsilon_2 > \varepsilon_1$) in all the figures show that when one of the films of the bilayer is viscous, the increase in ω_m is not that rapid with increase in the relaxation time of the viscoelastic film. Importantly, when λ_1 is increased under a viscous/viscoelastic upper layer, λ_m shifts from a lower to higher values when $\varepsilon_2 < \varepsilon_1$ and also when $\varepsilon_2 > \varepsilon_1$ (curve 1 to 4 in Figure 8(b)). In comparison, when λ_2 is varied at constant λ_1 , λ_m is found to marginally increase (decrease) when $\varepsilon_2 < \varepsilon_1$ ($\varepsilon_2 > \varepsilon_1$). Figure 8(e) shows that similar to the Kelvin-Voigt material, the Maxwell bilayer can also show a short- to long-wave transition when the film thickness is reduced from a few microns to a few nanometres.

C. Contact instabilities

The contact instabilities are engendered by the attractive interaction between the upper film and an approaching rigid contactor from the top, as shown schematically in Figure 1(c). The strength of the interaction is now governed by the ultrathin (<100 nm) air gap, rather than by the film thicknesses. Previously, Tomar *et al.*⁹³ have studied the contact instabilities of purely elastic bilayers and shown interesting interfacial morphologies through simulations. Importantly, for relatively thick single films,³⁸ the wavelength of instability is only dependent on the film thickness and independent of its elastic modulus. Tomar *et al.*⁹³ reported that for elastic bilayers, the length scale depends on the ratios of the film thicknesses and shear moduli. Thus, bilayers provide greater flexibility to control the length scale of patterns formed. The contact instabilities can be engendered in ultrathin to thick bilayers when the air gap between the contactor and the upper layer is kept ultrathin (<100 nm) and the van der Waals interaction is strong enough. In what follows, we consider both thin and relatively thick bilayers when discussing the key features of the contact instability induced by an external contactor. The bilayers considered here can be both elastomeric solids and Maxwell liquids. Figures 9–11 summarize the LSA results for the contact instability of viscoelastic bilayers.

1. Zero-frequency linear viscoelastic solid

The contact instabilities in viscoelastic bilayers can be experimented in two different pathways, (i) critical mode: when the contactor is gradually brought towards the bilayer from a large separation distance and the instability initiates when the destabilizing inter-surface attractive force marginally overcome the stabilizing forces, and (ii) dominant mode: the contactor is rapidly brought in the contact proximity such that the destabilizing force in the initial configuration is already much stronger than the stabilizing forces. In the former case, the instability is initiated following the wavelength λ_c ($=2\pi/k_c$) at the neutral stability condition ($\omega = 0$) and the instability evolves following the dominant wavelength λ_m ($=2\pi/k_m$) corresponding to ω_m in the later case.

Figures 9(a) and 9(b) show the neutral stability plots for elastomeric bilayers undergoing contact instability with $G_1 > G_2$ and $G_1 < G_2$, respectively. As in the case of electric field, the contact instability is initiated beyond a critical strength of the destabilizing attractive force (ϕ_c) with a wavelength λ_c . Figures 9(a)–9(d) show that this wavelength depends on the ratios of the thicknesses ($\beta = h_1/h_2$) and the ratio of shear moduli ($G_r = G_2/G_1$) of the films. When the films are of comparable thicknesses, the bifurcation diagrams show a single critical mode (curves 1 in Figures 9(a) and 9(b)). However, bimodal bifurcation diagrams are also observed when one of the layers is very thin (curves 2 and 3 in Figures 9(a) and 9(b)).

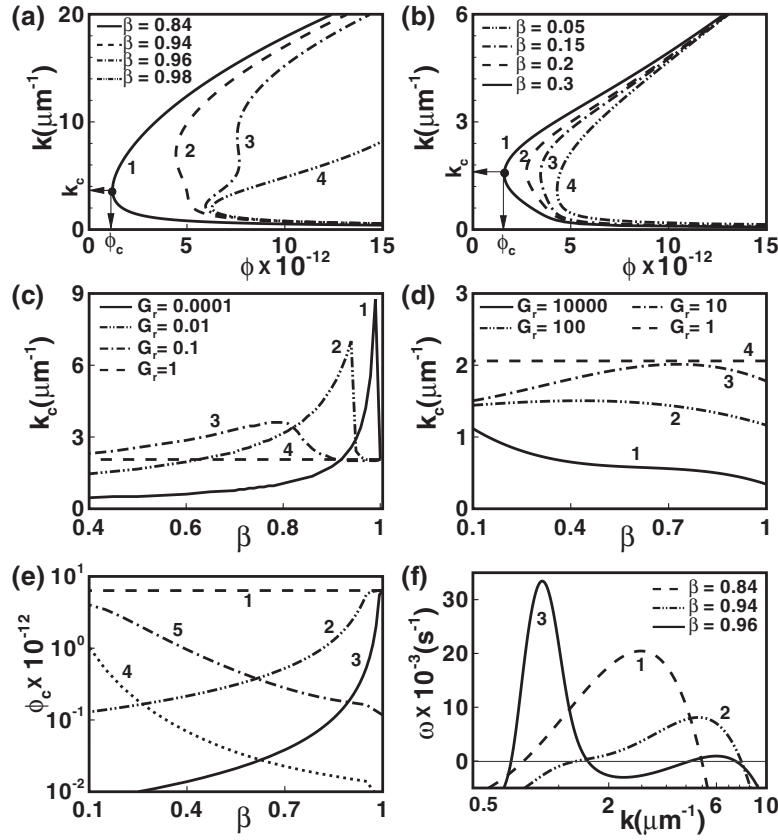


FIG. 9. LSA results for the contactor problem with zero frequency viscoelastic solid. Plots (a) [(b)] show the bifurcation diagrams (ϕ vs. k) when $G_1 = 10^6$ Pa and $G_2 = 10^4$ Pa [$G_1 = 10^4$ Pa and $G_2 = 10^6$ Pa] while β (h_{10}/h_{20}) is varied. Plot (c) [(d)] shows the variation of k_c with β at different $G_r = (G_2/G_1)$ and at constant $G_1 = 10^6$ Pa [$G_2 = 10^6$ Pa]. Plot (e) shows the variation of ϕ_c with β at different G_r . In plot (e) the curves 1-3, correspond to $G_r = 1, 0.01$ and 0.0001 , respectively when $G_1 = 10^6$ Pa and the curves 4 and 5, correspond to $G_r = 10000$ and 100 , respectively when $G_2 = 10^6$ Pa. Plot (f) shows the variation of ω with k when $G_1 = 10^6$ Pa and $G_2 = 10^4$ Pa. In all the plots, $h_{20} = 1 \mu\text{m}$, $\gamma_{21} = 0.00385$ N/m, $\gamma_2 = 0.03$ N/m, $A = 10^{-19}$ J, and $(d - h_{20}) = 7$ nm.

Figures 9(c) and 9(d) show that length scales of instability can be readily tailored by changing the ratio of shear moduli and film thicknesses. For example, when the bilayers have equal elastic modulus ($G_r = 1$) the instability evolves with the length scale similar to the single films ($k_c = 2.12$).³⁴ In comparison, when the upper layer is relatively thick and less elastic (curves 1 and 2 in Figure 9(c)) the length scale of instability is larger than the single layer length scale. However, a thinner and softer upper layer can evolve with a much smaller length scale as shown by the curves 1 and 2 in the Figure 9(c). Whereas when upper layer is more elastic than the lower layer, the length scale of instability is always larger than the single layer length scale (curves 1-4 in Figures 9(d)). Figure 9(e) shows that the critical force required to initiate instability in a bilayer (curves 2-5) is much smaller than for a single layer (broken line 1). The figure depicts that as the thickness of the film with the smaller shear modulus increases, ϕ_c progressively reduces because of the decreased elastic stiffness of the bilayer. The bimodal bifurcation plots shown in Figure 9(a) also correspond to finite wavenumber instabilities when the films evolve by picking up the dominant mode. The ω vs. k plots in Figure 9(f) clearly shows the bimodal nature of the contact instability, in which both the larger (curve 2) and smaller (curve 3) wavenumber maxima can be the dominant modes depending on the ratios of thicknesses and the shear moduli of the films.

Figure 10 shows the variations in ω_m and λ_m with the ratio of thicknesses and the shear moduli. Plot (a) shows that the ω_m rapidly reduces if the thickness of the film with larger elastic modulus is increased (curves 1, 4). Also, when the film is thin and less compliant, ω_m progressively decays

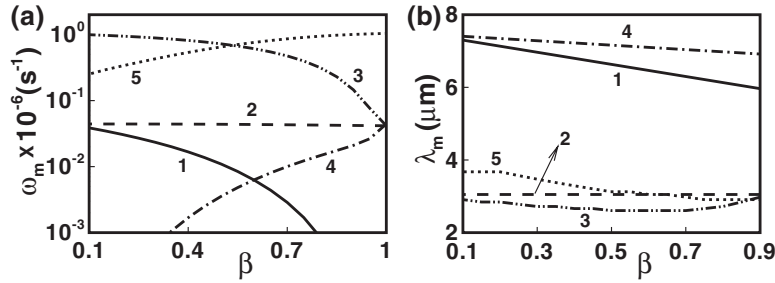


FIG. 10. LSA results for the contactor problem with zero-frequency viscoelastic solid. Plots (a) and (b) show the variations of ω_m and λ_m , respectively, with β at different $G_r = (G_2/G_1)$. The curves 1 and 4 correspond to $h_{20} = 100$ nm. The curves 2, 3, and 5 correspond to $h_{20} = 1$ μm . The curves 1 and 3 correspond to $G_r = 0.0001$ when $G_1 = 10^6$ Pa. The curve 2 corresponds to $G_r = 1$ and $G_1 = G_2 = 10^6$ Pa. The curves 4 and 5 correspond to $G_r = 10^4$ when $G_2 = 10^6$ Pa. In all the plots, $\gamma_{21} = 0.00385$ N/m, $\gamma_2 = 0.03$ N/m, $A = 10^{-19}$ J, and $(d - h_{20}) = 7$ nm.

(curves 3, 5). Plot (b) shows that by varying the thicknesses and shear moduli, a wide range of length scales can be achieved, including much larger to smaller length scales compared to the single films of similar configurations (broken line 2).

2. Maxwell fluid

In contrast to zero-frequency linear viscoelastic solid, the Maxwell fluids show long-wave contact instabilities as shown in the Figure 11. The curves 1-4 in the Figures 11(a) and 11(b) and the curves 1-3 in Figure 11(c) depict that with progressive increase in the relaxation time of any of the layers of a viscous-viscoelastic or a viscoelastic bilayer, ω_m rapidly increases. The sensitivity of λ_m with the relaxation times is also shown through the curves 1-3 in plot (d).

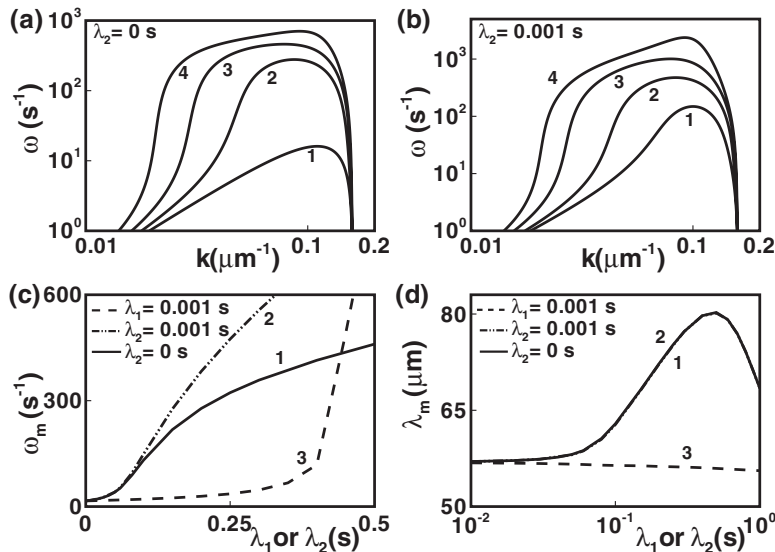


FIG. 11. LSA results for the contactor problem with Maxwell fluid bilayers. Plots (a) and (b) show the variation of ω with k . In plot (a) the curves 1–4 correspond to $\lambda_2 = 0$ s and $\lambda_1 = 0$ s, 0.2 s, 0.5 s, and 1.0 s, respectively. The curves 1–4 in plot (b) correspond to $\lambda_2 = 0.001$ s and $\lambda_1 = 0.1$ s, 0.25 s, 0.6 s, and 1.0 s, respectively. Plots (c) and (d) show the (i) variations of ω_m and λ_m , respectively, with λ_1 when $\lambda_2 = 0$ s (curve 1) and $\lambda_2 = 0.001$ s (curve 2) and (ii) variations of ω_m and λ_m , respectively, with λ_2 when $\lambda_1 = 0.001$ s (curve 3). For all plots $h_{30} = h_{10} = 1$ μm , $(d - h_{20}) = 50$ nm, $\gamma_2 = 0.04$ N/m, and $\gamma_{21} = 0.0007$ N/m.

V. CONCLUSIONS

We present a unified theory for thin viscoelastic bilayers undergoing wetting, electric field induced and contact induced instabilities. Under a single framework, the influences of rheological properties on the instabilities of two different types of linear viscoelastic materials, zero-frequency viscoelastic solid (characterized by its frequency independent elastic modulus and viscosity) and Maxwell fluid (characterized by its elastic relaxation time and viscosity) are discussed. The major conclusions are:

- (i) For the dewetting instability induced by the van der Waals forces, the bilayers are classified into three different cases depending on the individual dewetting and stability behavior of the two films. Only ultrathin (< 100 nm) bilayers can undergo a wetting instability and this instability is always long-wave for both Kelvin-Voigt and Maxwell materials owing to the overwhelming influence of interfacial tension. By changing the elasticity and the relaxation time of the films, the instabilities of one of the films can be suppressed or enhanced. For example, both the films can be unstable in the case 1 type bilayer. However, changing the shear modulus or relaxation time of the lower layer (upper layer) the instability can be shifted entirely to the upper layer (lower layer). It is observed that the switchover of the instabilities from one interface to the other leads to the significant change in the instability length scales. In the case 2 type bilayers, where the upper film is unstable on the stable lower film, the dominant mode of instability can still be switched from the upper to the lower interface or vice versa when the shear moduli or the relaxation times of the films are changed. In the case 3 type bilayers, where the lower film is unstable under a stable upper layer, show instability characteristics parallel to a single film as the rheological properties can only alter the time scale but not the length scale of instability.
- (ii) Similar to the van der Waals force induced instabilities, the viscoelastic films under the influence of electric field often show bimodality when the films have significantly dissimilar dielectric permittivities and interfacial tensions across the interfaces. However, a single wavelength mode at both the interfaces can be achieved when the dielectric contrast of the two films is not too large. The electric field induced instabilities for zero-frequency viscoelastic material has been found to be finite wavenumber instabilities that initiate beyond a critical applied field. The time and length scales of such instabilities can be altered by changing the elasticity of any of the layers and patterns with a wide range of length scales can be obtained as compared to similar single films. In contrast, the bilayers with Maxwell fluids are unconditionally unstable to any applied field owing to a lack of permanent elasticity. The dominant mode can be shifted from one interface to the other by changing the relaxation times of the films. Importantly, both the Kelvin-Voigt and Maxwell bilayers show a transition from the short- to long-waves when the film thickness is changed from a few hundred nm to a few micron because of decreased influence of the stabilizing surface tension force.
- (iii) Two different types of contact instabilities for bilayers are discussed. Firstly, for the critical mode, the length scales for the instabilities are identified from the neutral stability conditions and it is shown that the interfaces can deform in two different wavelengths when the lower layer is very thin and elastically stiff. In addition, unlike the single film scenario where the length scale is independent of the physical properties, the length scale for the bilayers is found to vary with the ratio of shear moduli and the thicknesses of the films. Further, presence of a compliant layer reduces the elastic stiffness of a bilayer, which helps it to undergo contact instability at a smaller applied contact force. Secondly, the dominant mode of contact instabilities in a bilayer is characterized when the destabilizing attractive interactions are initially much stronger than the stabilizing elastic and surface tension forces. The growth rate can show both mono-modal and bimodal characteristics - the latter engenders a sudden shift in the wavelength for small changes in the parameters. The contact instabilities for Maxwell fluid bilayers are always found to have long-wave characteristics and show that variations in the relaxation times of the layers can greatly alter the length and the time scale of instabilities.
- (iv) For all the spinodal instabilities, the length and time scales change significantly with the ratio of shear moduli or the elastic relaxation time of the films. This is in contrast to the single film systems where the length scale is independent of the rheological properties of the films. Thus,

viscoelastic bilayers provide far more flexibility in tuning the wavelength as compared to the single film systems. The Kelvin-Voigt viscoelastic bilayer always shows a finite wavenumber bifurcation at a critical destabilizing force. However, replacing any of the layers with a viscous layer removes the elastic-stiffness and thus it becomes unstable to vanishingly small field strengths. Purely Maxwell bilayers are also unstable to vanishingly small fields with critical wavenumber approaching zero.

In summary, the general theory and the linear stability analysis presented here addresses many interesting scenarios of instabilities in thin viscoelastic bilayers made unstable by the van der Waals forces and electric fields that are of interest in a host of applications such as self-organized patterning, multilayer coatings, micro- and nano-fluidics. The detailed morphology of the nonlinear patterns beyond the onset of instability has to be addressed by nonlinear simulations, which need to be investigated in future.

ACKNOWLEDGMENTS

D.B. acknowledges initiation grant from IIT Guwahati and a Fast-Track research grant SR/FTP/ETA-091/2009 from DST India. A.S. acknowledges the support from the Ministry of Education, Science and Technology, South Korea under the World Class University (WCU) program R32-2008-000-20082-0 and from the DST Unit on Soft Nanofabrication at IITK.

APPENDIX: DISPERSION RELATIONS

The dispersion relation for the zero-frequency viscoelastic solid:

$$\begin{vmatrix} 1 & -1 & \frac{1}{k} & \frac{1}{k} & 0 & 0 & 0 & 0 \\ 1 & 1 & 0 & 0 & 0 & 0 & 0 & 0 \\ P_1 & -P_2 & \frac{P_1 P_5}{k} & -\frac{P_2 P_6}{k} & -P_1 & P_2 & -\frac{P_1 P_5}{k} & \frac{P_2 P_6}{k} \\ P_1 & P_2 & h_1 P_1 & h_1 P_2 & -P_1 & -P_2 & -h_1 P_1 & -h_1 P_2 \\ k P_1 P_{14} & k P_2 P_{14} & k P_1 P_5 P_{14} & k P_2 P_6 P_{14} & -k P_1 P_{15} & -k P_2 P_{15} & -P_1 P_5 P_{15} & -P_2 P_6 P_{15} \\ 0 & 0 & 0 & 0 & k P_3 P_{15} & k P_4 P_{15} & P_3 P_7 P_{15} & P_4 P_8 P_{15} \\ P_1 P_9 & P_2 P_{10} & P_1 P_9 h_1 & P_2 P_{10} h_2 & P_{16} & P_{17} & P_{18} & P_{19} \\ P_1 \phi_2 & P_2 \phi_2 & h_1 P_1 \phi_2 & h_1 P_2 \phi_2 & P_3 P_{12} & P_4 P_{11} & h_2 P_3 P_{12} & h_2 P_4 P_{11} \end{vmatrix} = 0, \quad (\text{A1})$$

where $P_1 = e^{kh_1}$; $P_2 = e^{-kh_1}$; $P_3 = e^{kh_2}$; $P_4 = e^{-kh_2}$; $P_5 = (1 + kh_1)$; $P_6 = (-1 + kh_1)$; $P_7 = (1 + kh_2)$; $P_8 = (-1 + kh_2)$; $P_9 = -2kG_1 - 2k\omega\mu_1 + \phi_1$; $P_{10} = 2kG_1 + 2k\omega\mu_1 + \phi_1$; $P_{11} = 2kG_2 + 2k\omega\mu_2 + \phi_4$; $P_{12} = -2kG_2 - 2k\omega\mu_2 + \phi_4$; $-P_{13} = 2kG_2 2k\omega\mu_2 - \phi_4$; $P_{14} = G_1 + \omega\mu_1$; $P_{15} = G_2 + \omega\mu_2$; $P_{16} = 2kG_2 P_1 + 2k\omega P_1 \mu_2 + P_3 \phi_2$; $P_{17} = -2kG_2 P_2 - 2k\omega P_2 \mu_2 + P_4 \phi_2$; $P_{18} = -2kG_2 h_1 P_1 + 2k\omega h_1 P_1 \mu_2 + h_2 P_3 \phi_2$; $P_{19} = -2kG_2 h_1 P_2 - 2k\omega h_1 P_2 \mu_2 + h_2 P_4 \phi_2$; $\phi_1 = (-\gamma_{21} k^2 + [\partial\pi_1/\partial h_1] - [\partial\pi_2/\partial h_1])$; $\phi_2 = (\partial\pi_2/\partial h_1)$; $\phi_4 = -\gamma_2 k^2 + [\partial\pi_2/\partial h_2]$.

The dispersion relation for the Maxwell fluid:

$$\begin{vmatrix} 1 & -1 & \frac{1}{k} & \frac{1}{k} & 0 & 0 & 0 & 0 \\ 1 & 1 & 0 & 0 & 0 & 0 & 0 & 0 \\ -P_1 & P_2 & -\frac{P_1 P_5}{k} & \frac{P_2 P_6}{k} & P_1 & -P_2 & \frac{P_1 P_5}{k} & -\frac{P_2 P_6}{k} \\ P_1 & P_2 & h_1 P_1 & h_1 P_2 & -P_1 & -P_2 & -h_1 P_1 & -h_1 P_2 \\ \frac{k P_1 \mu_1}{P_9} & \frac{k P_2 \mu_1}{P_9} & \frac{\mu_1 P_1 P_5}{P_9} & \frac{\mu_1 P_2 P_6}{P_9} & -\frac{k \mu_2 P_1}{P_{10}} & -\frac{k \mu_2 P_2}{P_{10}} & -\frac{\mu_2 P_1 P_5}{P_{10}} & -\frac{\mu_2 P_2 P_6}{P_{10}} \\ 0 & 0 & 0 & 0 & \frac{k P_3 \mu_2}{P_{10}} & \frac{k P_4 \mu_2}{P_{10}} & \frac{P_3 P_7 \mu_2}{P_{10}} & \frac{\mu_2 P_4 P_8}{P_{10}} \\ P_1 P_{11} & P_2 P_{12} & \frac{h_1 P_1 P_{13}}{\omega P_9} & \frac{h_1 P_2 P_{14}}{\omega P_9} & P_{15} & P_{16} & P_{17} & P_{18} \\ \frac{P_1 \varphi_2}{\omega} & \frac{P_2 \varphi_2}{\omega} & \frac{h_1 P_1 \varphi_2}{\omega} & \frac{h_1 P_2 \varphi_2}{\omega} & P_3 P_{19} & P_4 P_{20} & \frac{h_2 P_3 P_{21}}{\omega P_{10}} & \frac{h_2 P_4 P_{22}}{\omega P_{10}} \end{vmatrix} = 0. \quad (\text{A2})$$

Here $P_1 = e^{kh_1}$; $P_2 = e^{-kh_1}$; $P_3 = e^{kh_2}$; $P_4 = e^{-kh_2}$; $P_5 = (1 + kh_1)$; $P_6 = (-1 + kh_1)$; $P_7 = (1 + kh_2)$; $P_8 = (-1 + kh_2)$; $P_9 = 1 + \omega\lambda_1$; $P_{10} = 1 + \omega\lambda_2$; $P_{11} = -2k\mu_1/P_9 + \phi_1/\omega$; $P_{12} = 2k\mu_1/P_9 + \phi_1/\omega$; $P_{13} = -2k\omega\mu_1 + P_9\phi_1$; $P_{14} = 2k\omega\mu_1 + P_9\phi_1$; $P_{15} = 2kP_1\mu_2/P_{10} + P_3\phi_2/\omega$; $P_{16} = -2kP_2\mu_2/P_{10} + P_4\phi_2/\omega$; $P_{17} = 2kh_1P_1\mu_2/P_{10} + h_2P_3\phi_2/\omega$; $P_{18} = -2kh_1P_2\mu_2/P_{10} + h_2P_4\phi_2/\omega$; $P_{19} = -2k\mu_2/P_{10} + \phi_4/\omega$; $P_{20} = 2k\mu_2/P_{10} + \phi_4/\omega$; $P_{21} = -2k\omega\mu_2 + P_{10}\phi_4$; $P_{22} = 2k\omega\mu_2 + P_{10}\phi_4$; $\phi_1 = (-\gamma_{21}k^2 + [\partial\pi_1/\partial h_1] - [\partial\pi_2/\partial h_1])$; $\phi_2 = (\partial\pi_2/\partial h_1)$; $\phi_4 = -\gamma_2k^2 + [\partial\pi_2/\partial h_2]$.

- ¹ P. G. De Gennes, "Wetting: Statics and dynamics," *Rev. Mod. Phys.* **57**, 827 (1985).
- ² C. J. van Oss, M. K. Chaudhury, and R. Good, "Interfacial Lifshitz-van der Waals and polar interactions in macroscopic systems," *Chem. Rev. (Washington, D.C.)* **88**, 927 (1988).
- ³ A. Oron, S. H. Davis, and S. G. Bankoff, "Long-scale evolution of thin liquid films," *Rev. Mod. Phys.* **69**, 931 (1997).
- ⁴ R. V. Craster and O. K. Matar, "Dynamics and stability of thin liquid films," *Rev. Mod. Phys.* **81**, 1131 (2009).
- ⁵ E. Ruckenstein, and R. K. Jain, "Spontaneous rupture of thin liquid films," *Faraday Trans.* **70**, 132 (1974).
- ⁶ M. B. Williams, and S. H. Davis, "Nonlinear theory of film rupture," *J. Colloid Interface Sci.* **90**, 220 (1982).
- ⁷ G. Reiter, "Dewetting of thin polymer films," *Phys. Rev. Lett.* **68**, 75 (1992).
- ⁸ G. Reiter, "Unstable thin polymer films: Rupture and dewetting processes," *Langmuir* **9**, 1344 (1993).
- ⁹ S. Herminghaus, K. Jacobs, K. Mecke, J. Bischof, A. Fery, M. Ibn-Elhaj, and S. Schlagowski, "Spinodal dewetting in liquid crystal and liquid metal films," *Science* **282**, 916 (1998).
- ¹⁰ R. Seemann, S. Herminghaus, and K. Jacobs, "Dewetting patterns and molecular forces: A reconciliation," *Phys. Rev. Lett.* **86**, 5534 (2001).
- ¹¹ A. Sharma, "Relationship of thin film stability and morphology to macroscopic parameters of wetting in the apolar and polar systems," *Langmuir* **9**, 861 (1993).
- ¹² A. Sharma and R. Khanna, "Pattern formation in unstable thin liquid films," *Phys. Rev. Lett.* **81**, 3463 (1998).
- ¹³ A. Oron, "Three-dimensional nonlinear dynamics of thin liquid films," *Phys. Rev. Lett.* **85**, 2108 (2000).
- ¹⁴ G. Reiter, P. Auroy, and L. Auvray, "Instability of thin polymer films on layers of chemically identical grafted molecules," *Macromolecules* **29**, 2150 (1996).
- ¹⁵ R. Konnur, K. Kargupta, and A. Sharma, "Instability and morphology of thin liquid films on chemically heterogeneous substrates," *Phys. Rev. Lett.* **84**, 931 (2000).
- ¹⁶ U. Thiele, M. Velarde, and K. Neuffer, "Dewetting: Film rupture by nucleation in the spinodal regime," *Phys. Rev. Lett.* **87**, 016104 (2001).
- ¹⁷ K. Kargupta and A. Sharma, "Templating of thin films induced by dewetting on patterned surfaces," *Phys. Rev. Lett.* **86**, 4536 (2001).
- ¹⁸ A. Sehgal, V. Ferreiro, J. F. Douglas, E. J. Amis, and A. Karim, "Pattern-directed dewetting of ultrathin polymer films," *Langmuir* **18**, 7041 (2002).
- ¹⁹ R. Mukherjee, D. Bandyopadhyay, and A. Sharma, "Control of morphology in pattern directed dewetting of thin polymer films," *Soft Matter* **4**, 2086 (2008).
- ²⁰ L. Bruschi, H. Kühne, U. Thiele, and M. Bär, "Dewetting of thin films on heterogeneous substrates: Pinning versus coarsening," *Phys. Rev. E* **66**, 011602 (2002).
- ²¹ U. Thiele, L. Bruschi, M. Bestehorn, and M. Bär, "Modeling thin-film dewetting on structured substrates and templates: Bifurcation analysis and numerical simulations," *Eur. Phys. J. E* **11**, 255 (2003).
- ²² J. C. T. Kao, A. A. Golovin, and S. H. Davis, "Rupture of thin films with resonant substrate patterning," *J. Colloid Interface Sci.* **303**, 532 (2006).
- ²³ D. Simmons and A. Chauhan, "Influence of physical and chemical heterogeneity shape on thin film rupture," *J. Colloid Interface Sci.* **295**, 472 (2006).
- ²⁴ S. Saprykin, P. M. J. Trevelyan, R. J. Koopmans, and S. Kalliadasis, "Free-surface thin-film flows over uniformly heated topography," *Phys. Rev. E* **75**, 026306 (2007).
- ²⁵ T. Erneux and S. H. Davis, "Nonlinear Rupture of free films," *Phys. Fluids* **5**, 1117 (1993).
- ²⁶ A. Sharma and K. Kargupta, "Instability and dynamics of thin slipping films," *App. Phys. Lett.* **83**, 3549 (2003).
- ²⁷ S. A. Safran and J. Klein, "Surface instability of viscoelastic thin films," *J. Phys. II France* **3**, 749 (1993).
- ²⁸ S. Herminghaus, R. Seemann, and K. Jacobs, "Generic morphology of viscoelastic dewetting fronts," *Phys. Rev. Lett.* **89**, 056101-1 (2002).
- ²⁹ M. Rauscher, A. Münch, B. Wagner, and R. Blossey, "A thin-film equation for viscoelastic liquids of Jeffrey's type," *Eur. Phys. J. E* **17**, 373 (2005).
- ³⁰ J. Sarkar and A. Sharma, "A unified theory of instabilities in viscoelastic thin films: From wetting to confined films, from viscous to elastic films, and from short to long waves," *Langmuir* **26**, 8464 (2010).
- ³¹ G. Tomar, V. Shankar, S. K. Shukla, A. Sharma, and G. Biswas, "Instability and dynamics of thin viscoelastic liquid films," *Eur. Phys. J. E* **20**, 185 (2006).
- ³² A. Patra, D. Bandyopadhyay, G. Tomar, A. Sharma, and G. Biswas, "Instability and dewetting of ultrathin solid viscoelastic films on homogeneous and heterogeneous substrates," *J. Chem. Phys.* **134**, 064705 (2011).
- ³³ A. Ghatak, M. Chaudhury, V. Shenoy, and A. Sharma, "Meniscus instability in confined thin elastic films," *Phys. Rev. Lett.* **85**, 4329 (2000).
- ³⁴ V. Shenoy and A. Sharma, "Pattern formation in a thin solid film with interactions," *Phys. Rev. Lett.* **86**, 119 (2001).
- ³⁵ V. Shenoy and A. Sharma, "Stability of a thin elastic film interacting with a contactor," *J. Mech. Phys. Solids* **50**, 1155 (2002).
- ³⁶ C. Q. Ru, "Surface wrinkling of two mutually attracting elastic thin films due to van der Waals forces," *J. Appl. Phys.* **90**, 6098 (2001).

- ³⁷W. Mönch and S. Herminghaus, "Elastic instability of rubber films between solid bodies," *Europhys. Lett.* **53**, 525 (2001).
- ³⁸J. Sarkar, V. Shenoy, and A. Sharma, "Patterns, forces and metastable pathways in debonding of elastic films," *Phys. Rev. Lett.* **93**, 018302 (2004).
- ³⁹M. Gonuguntala, A. Sharma, J. Sarkar, S. A. Subramanian, M. Ghosh, and V. Shenoy, "Contact instability in adhesion and debonding of thin elastic films," *Phys. Rev. Lett.* **97**, 018303 (2006).
- ⁴⁰M. Gonuguntala, A. Sharma, R. Mukharjee, and S. A. Subramanian, "Control of self-organized contact instability and patterning in soft elastic films," *Langmuir* **22**, 7066 (2006).
- ⁴¹E. Schäffer, T. Thurn-Albrecht, T. P. Russell, and U. Steiner, "Electrically induced structure formation and pattern transfer," *Nature (London)* **403**, 874 (2000).
- ⁴²J. W. Swan, "Stress and other effects produced in resin and in a viscid compound of resin and oil by electrification," *Proc. R. Soc. London* **62**, 38 (1897).
- ⁴³G. I. Taylor and A. D. McEwan, "The stability of a horizontal fluid interface in a vertical electric field," *J. Fluid Mech.* **22**, 1 (1965).
- ⁴⁴J. R. Melcher and C. V. Smith, "Electrohydrodynamic charge relaxation and interfacial perpendicular-field instability," *Phys. Fluids* **12**, 778 (1969).
- ⁴⁵D. A. Saville, "Electrohydrodynamics: The Taylor-Melcher leaky dielectric model," *Annu. Rev. Fluid Mech.* **29**, 27 (1997).
- ⁴⁶P. Deshpande, X. Sun, and S. Y. Chou, "Observation of dynamic behavior of lithographically induced self-assembly of supramolecular periodic pillar arrays in a homopolymer film," *Appl. Phys. Lett.* **79**, 1688 (2001).
- ⁴⁷L. F. Pease and W. B. Russel, "Electrostatically induced submicron patterning of thin perfect and leaky dielectric films: A generalized linear stability analysis," *J. Chem. Phys.* **118**, 3790 (2003).
- ⁴⁸N. Wu, L. F. Pease, and W. B. Russel, "Electric-field-induced patterns in thin polymer films: Weakly nonlinear and fully nonlinear evolution," *Langmuir* **21**, 12290 (2005).
- ⁴⁹N. Wu, L. F. Pease, and W. B. Russel, "Toward large-scale alignment of electro hydrodynamic patterning of thin polymer films," *Adv. Funct. Mater.* **16**, 1992 (2006).
- ⁵⁰R. Verma, A. Sharma, K. Kargupta, and J. Bhaumik, "Electric field induced instability and pattern formation in thin liquid films," *Langmuir* **21**, 3710 (2005).
- ⁵¹S. Harkema and U. Steiner, "Hierarchical pattern formation in thin polymer films using an electric field and vapor sorption," *Adv. Funct. Mater.* **15**, 2016 (2005).
- ⁵²D. Tseluiko, M. G. Blyth, D. T. Papageorgiou, and J.-M. Vanden-Broeck, "Electrified viscous thin film flow over topography," *J. Fluid Mech.* **597**, 449 (2008).
- ⁵³S. Herminghaus, "Dynamical instability of thin liquid films between conducting media," *Phys. Rev. Lett.* **83**, 2359 (1999).
- ⁵⁴Z. Q. Lin, T. Kerle, S. M. Baker, D. A. Hoagland, E. Schäffer, U. Steiner, and T. P. Russell, "Electric field induced instabilities at liquid/liquid interfaces," *J. Chem. Phys.* **114**, 2377 (2001).
- ⁵⁵Z. Q. Lin, T. Kerle, T. P. Russell, E. Schäffer, and U. Steiner, "Structure formation at the interface of liquid/liquid bilayer in electric field," *Macromolecules* **35**, 3971 (2002).
- ⁵⁶Z. Q. Lin, T. Kerle, T. P. Russell, E. Schäffer, and U. Steiner, "Electric field induced dewetting at polymer/polymer interfaces," *Macromolecules* **35**, 6255 (2002).
- ⁵⁷V. Shankar and A. Sharma, "Instability of the interface between thin fluid films subjected to electric fields," *J. Colloid Interface Sci.* **274**, 294 (2004).
- ⁵⁸R. V. Craster and O. K. Matar, "Electrically induced pattern formation in thin leaky dielectric films," *Phys. Fluids* **17**, 032104 (2005).
- ⁵⁹G. Tomar, V. Shankar, A. Sharma, and G. Biswas, "Electrohydrodynamic instability of a confined viscoelastic liquid film," *J. Non-Newtonian Fluid Mech.* **143**, 120 (2007).
- ⁶⁰N. Arun, A. Sharma, P. S. G. Pattader, I. Banerjee, H. M. Dixit, and K. S. Narayan, "Electric-field-induced patterns in soft viscoelastic films: From long-waves of viscous liquids to short-waves of elastic solids," *Phys. Rev. Lett.* **102**, 254502 (2009).
- ⁶¹J. Sarkar, A. Sharma, and V. Shenoy, "Electric-field induced instabilities and morphological phase transitions in soft elastic films," *Phys. Rev. E* **77**, 031604 (2008).
- ⁶²C. H. Maldarelli, R. K. Jain, I. B. Ivanov, and E. Ruckenstein, "Stability of symmetric and unsymmetric thin liquid films to short and long wavelength perturbations," *J. Colloid Interface Sci.* **78**, 118 (1980).
- ⁶³P. Lambooy, K. C. Phelan, O. Haugg, and G. Krausch, "Dewetting at the Liquid-Liquid interface," *Phys. Rev. Lett.* **76**, 1110 (1996).
- ⁶⁴Q. Pan, I. K. Winey, H. H. Hu, and R. J. Composto, "Unstable polymer bilayers. 2. The effect of film thickness," *Langmuir* **13**, 1758 (1997).
- ⁶⁵R. A. Segalman and P. F. Green, "Dynamics of rims and the onset of spinodal dewetting at liquid/liquid interfaces," *Macromolecules* **32**, 801 (1999).
- ⁶⁶H. Kang, S. H. Lee, S. Kim, and K. Char, "Dewetting and layer inversion of inverted PVP/PS bilayer films," *Macromolecules* **36**, 8579 (2003).
- ⁶⁷J. P. de Silva, M. Geoghegan, A. M. Higgins, G. Krausch, M. O. David, and G. Reiter, "Switching layer stability in a polymer bilayer by thickness variation," *Phys. Rev. Lett.* **98**, 267802 (2007).
- ⁶⁸A. M. Higgins and R. A. L. Jones, "Anisotropic spinodal dewetting as a route to self-assembly of patterned surfaces," *Nature (London)* **404**, 476 (2000).
- ⁶⁹O. Wunnicke, P. Müller-Buschbaum, M. Wolkenhauer, C. Lorenz-Haas, R. Cubitt, V. Leiner, and M. Stamm, "Stabilization of thin polymeric bilayer films on top of semiconductor surfaces," *Langmuir* **19**, 8511 (2003).
- ⁷⁰J. LeOpoldes and P. Damman, "From a two-dimensional chemical pattern to a three-dimensional topology through selective inversion of a liquid-liquid bilayer," *Nat. Mater.* **5**, 957 (2006).

- ⁷¹ K. D. Danov, V. N. Paunov, N. Alleborn, H. Raszillier, and F. Durst, "Stability of evaporating two-layered liquid film in the presence of surfactant-I. The equations of lubrication approximation - III. Nonlinear stability analysis," *Chem. Eng. Sci.* **53**, 2809 (1998).
- ⁷² K. D. Danov, V. N. Paunov, S. D. Stoyanov, N. Alleborn, H. Raszillier, and F. Durst, "Stability of evaporating two-layered liquid film in the presence of surfactant-II. Linear analysis - III. Nonlinear stability analysis," *Chem. Eng. Sci.* **53**, 2823 (1998).
- ⁷³ V. N. Paunov, K. D. Danov, N. Alleborn, H. Raszillier, and F. Durst, "Stability of evaporating two-layered liquid film in the presence of surfactant-III. Non-linear stability analysis," *Chem. Eng. Sci.* **53**, 2839 (1998).
- ⁷⁴ A. Pototsky, M. Bestehorn, D. Merkt, and U. Thiele, "Alternative pathways of dewetting for a thin liquid two-layer film," *Phys. Rev. E* **70**, 025201 (2004).
- ⁷⁵ A. Pototsky, M. Bestehorn, D. Merkt, and U. Thiele, "Morphology changes in the evolution of liquid two-layer films," *J. Chem. Phys.* **122**, 224711 (2005).
- ⁷⁶ A. Pototsky, M. Bestehorn, D. Merkt, and U. Thiele, "Evolution of interface patterns of three-dimensional two-layer liquid films," *Euro. Phys. Lett.* **74**, 665 (2006).
- ⁷⁷ L. S. Fisher and A. A. Golovin, "Nonlinear stability analysis of a two-layer thin liquid film: Dewetting and autophobic behavior," *J. Colloid Interface Sci.* **291**, 515 (2005).
- ⁷⁸ L. S. Fisher and A. A. Golovin, "Instability of a two-layer thin liquid film with surfactants: Dewetting waves," *J. Colloid Interface Sci.* **307**, 203 (2007).
- ⁷⁹ D. Bandyopadhyay, R. Gulabani, and A. Sharma, "Instability and dynamics of thin liquid Bilayers," *Ind. Engg. Chem. Res.* **44**, 1259 (2005).
- ⁸⁰ D. Bandyopadhyay and A. Sharma, "Nonlinear instabilities and pathways of rupture in thin liquid Bilayers," *J. Chem. Phys.* **125**, 054711 (2006).
- ⁸¹ D. Bandyopadhyay and A. Sharma, "Dewetting pathways and morphology of unstable thin liquid bilayers," *J. Phys. Chem. B* **112**, 11564 (2008).
- ⁸² L. Xu, D. Bandyopadhyay, A. Sharma, and S. W. Joo, "Switching of interfacial instabilities from the liquid/air interface to the liquid/liquid interface in a polymer," *Soft Matter* **7**, 8056 (2011).
- ⁸³ L. Xu, D. Bandyopadhyay, T. Shi, L. An, A. Sharma, and S. W. Joo, "Dewetting kinetics of thin polymer bilayers: Role of under layer," *Polymer* **52**, 4345 (2011).
- ⁸⁴ D. Bandyopadhyay, A. Sharma, and C. Rastogi, "Dewetting of the thin liquid bilayers on topographically patterned substrates: Formation of microchannel and microdot arrays," *Langmuir* **24**, 14048 (2008).
- ⁸⁵ D. Bandyopadhyay and A. Sharma, "Self-organized microstructures in thin bilayers on chemically patterned substrates," *J. Phys. Chem. C* **114**, 2237 (2010).
- ⁸⁶ A. A. Nepomnyashchy and I. B. Simanovskii, "Convective flows in a two-layer system with a temperature gradient along the interface," *Phys. Fluids* **18**, 032105 (2006).
- ⁸⁷ A. A. Nepomnyashchy and I. B. Simanovskii, "Decomposition of a two-layer thin liquid film flowing under the action of Marangoni stresses," *Phys. Fluids* **18**, 112101 (2006).
- ⁸⁸ A. A. Nepomnyashchy and I. B. Simanovskii, "Instabilities and ordered patterns in nonisothermal ultrathin bilayer fluid films," *Phys. Rev. Lett.* **102**, 164501 (2009).
- ⁸⁹ A. Martin, O. Rossier, A. Buguin, P. Auroy, and F. Brochard-Wyart, "Spinodal dewetting of thin liquid films at soft interfaces," *Euro. Phys. J. E* **3**, 337 (2000).
- ⁹⁰ S. Kumar and O. K. Matar, "Dewetting of thin liquid films near soft elastomeric layers," *J. Colloid Interface Sci.* **273**, 581 (2004).
- ⁹¹ O. K. Matar, V. Gkanis, and S. Kumar, "Nonlinear evolution of thin liquid films dewetting near soft elastomeric layers," *J. Colloid Interface Sci.* **286**, 319 (2005).
- ⁹² J. Yoon, C. Q. Ru, and A. Midouchowski, "Surface instability of a bilayer elastic film due to surface van der Waals forces," *J. Appl. Phys.* **98**, 113503 (2005).
- ⁹³ G. Tomar, A. Sharma, V. Shenoy, and G. Biswas, "Surface instability of confined elastic bilayers: Theory and simulations," *Phys. Rev. E* **76**, 011607 (2007).
- ⁹⁴ R. Mukherjee, R. Pangule, A. Sharma, and G. Tomar, "Contact instability of elastic bilayers: Miniaturization of instability patterns," *Adv. Func. Mat.* **17**, 2356 (2007).
- ⁹⁵ D. Bandyopadhyay, A. Sharma, and V. Shankar, "Electric field and contact force induced tunable patterns in slipping soft elastic films," *Euro Phys. Lett.* **89**, 36002 (2010).
- ⁹⁶ M. D. Morariu, N. E. Voicu, E. Schaffer, Z. Lin, T. P. Russel, and U. Steiner, "Hierarchical structure formation and pattern replication induced by an electric field," *Nat. Mater.* **2**, 48 (2003).
- ⁹⁷ K. A. Leach, S. Gupta, M. D. Dickey, C. G. Wilson, and T. P. Russell, "Electric field and dewetting induced hierarchical structure formation in polymer-polymer-air trilayers," *Chaos* **15**, 047506 (2005).
- ⁹⁸ D. Bandyopadhyay, A. Sharma, U. Thiele, and P. D. S. Reddy, "Electric field induced instabilities and interfacial morphologies of thin viscous and elastic Bilayers," *Langmuir*, **25**, 9108 (2009).
- ⁹⁹ P. D. S. Reddy, D. Bandyopadhyay, and A. Sharma, "Self-organized ordered arrays of core-shell columns in viscous bilayers formed by spatially varying electric fields," *J. Phys. Chem. C* **114**, 21020 (2010).
- ¹⁰⁰ S. A. Roberts and S. Kumar, "AC electrohydrodynamic instabilities in thin liquid films," *J. Fluid Mech.* **631**, 255 (2009).
- ¹⁰¹ S. A. Roberts and S. Kumar, "Electrohydrodynamic instabilities in thin liquid trilayer films," *Phys. Fluids* **22**, 122102 (2010).